Chapter 3

THE LAVIC LAKE FAULT: A LONG TERM CUMULATIVE SLIP ANALYSIS VIA COMBINED FIELD WORK AND THERMAL HYPERSPECTRAL AIRBORNE REMOTE SENSING

Rebecca A. Witkosky[1], Joann M. Stock[1], David M. Tratt[2], Kerry N. Buckland[2], Paul M. Adams[2], Patrick D. Johnson[2], David K. Lynch[2], and Francis J. Sousa[3]

[1]*California Institute of Technology, Division of Geological and Planetary Sciences, 1200 E. California Blvd., MC 170-25, Pasadena CA 91125*

[2]*The Aerospace Corporation, 2310 E. El Segundo Blvd., El Segundo CA 90245*

[3]*Oregon State University, College of Earth, Ocean, and Atmospheric Sciences, 104 CEOAS Administration Building, Corvallis, OR 97331-5503*

ABSTRACT

The 1999 Mw 7.1 Hector Mine earthquake was a major surface-rupturing event in the Mojave Desert region of eastern California, with coseismic right-lateral slip in excess of 5 m along the Lavic Lake fault. The cumulative long-term bedrock offset and geologic slip rate of this fault are not well defined, which inhibits tectonic reconstructions of the Eastern California shear zone (ECSZ). Furthermore, access to the fault is restricted, which complicates field work to study the fault's geological history. We gained access to the area in 2012 and 2014 to collect new field data, and in 2013, we collected new thermal

hyperspectral airborne imagery with a 2 m pixel size. With this new data, and auxiliary information from older geologic maps, we created lithologic maps of the area using supervised and unsupervised classifications of the remote sensing imagery. Based on our own field observations, we defined end member rock classes for the supervised classifications over a small test area. The high spatial and spectral resolution of the airborne sensor, along with a lack of significant vegetation, allowed us to optimize a data processing sequence for supervised classifications, resulting in lithologic maps of the test area with an overall accuracy of 71 ± 1%. For the unsupervised classifications, we first relied on an algorithm to define classes based on spectral information within the complete swath of remote sensing imagery, and then assigned rock types to these classes using information from a previous map of the area. To identify bedrock offset by the fault, we used the unsupervised lithologic classification map. A boundary between units in our unsupervised classification map correlated very well with a lithologic boundary that is displaced by the fault in a previously published geologic map. The lithologic boundary, a depositional contact between two volcanic units, pre-dates the Lavic Lake fault, thus capturing the entire cumulative long-term offset. We used the displaced depositional contact to calculate the vertical component of slip along the main Lavic Lake fault, and an older cross fault to measure the horizontal component of slip along the main fault. We then combined the vertical and horizontal components to derive a net fault slip of 960 +70/-40 m. We interpret that value as a maximum due to uncertainty in the dip angle of the cross fault. Our value is significantly less than a previous estimate of cumulative offset (3.4 ± 0.8 km) that was based on an offset magnetic feature, which we suggest may be partially due to off-fault deformation along proximal, smaller ECSZ structures. Our data corroborate past suggestions that transient tectonic

activity in the ECSZ may be responsible for the observed discrepancy between the higher current, measured geodetic slip rate and the total geologic rate since ~750 ka.

INTRODUCTION

The 1992 Mw 7.3 Landers and 1999 M_w 7.1 Hector Mine earthquakes resulted in two major surface ruptures in the Mojave Desert region of eastern California (Figure 1). The faults that ruptured in the 1992 Landers event were mostly located on publicly accessible land, allowing considerable subsequent geologic investigation (e.g. Sieh et al., 1993; Johnson et al., 1993; Arrowsmith and Rhodes, 1994; Unruh et al., 1994; Spotila and Sieh, 1995; Zachariasen and Sieh, 1995; Savage and Svarc, 1997; McGill and Rubin, 1999; Rockwell et al., 2000). However, faults that ruptured in the 1999 Hector Mine event (Figure 1), which include the Lavic Lake fault, and portions of the Calico-Hidalgo, Mesquite Lake, Pisgah-Bullion faults (Figure 2A), lie within the United States Marine Corps Air Ground Combat Center (MCAGCC), Twentynine Palms, and therefore received only limited field-based study (Treiman et al., 2002).

Remote sensing methods can yield additional useful data for studying these faults. The coseismic slip of the 1999 Hector Mine earthquake has been investigated with several remote sensing methods: InSAR from Fialko and Simons (2001); InSAR from Sandwell et al. (2002); InSAR and GPS from Simons et al. (2002); lidar-based offset measurements from Hudnut et al. (2002); lidar-based offset measurements from Chen et al. (2015); lidar-based (as well as field-based) offset measurements from Sousa (2016). Results of these studies generally concur with the principal field-based slip measurements (Treiman et al., 2002).

In this paper we use a new and more detailed remote sensing data set, thermal hyperspectral airborne imagery, to produce a geologic swath map and estimate the cumulative long-term tectonic offset of bedrock along the Lavic Lake fault. With this imagery, it is possible to differentiate various minerals and lithology within a scene by comparison of their spectra via supervised and unsupervised classifications. These are algorithmic classification methods for grouping pixels in an image by quantifying and comparing spectral similarity. We first used supervised classifications, which require the user to have some knowledge of ground cover (for lithologic mapping, the composition of rocks exposed at the surface) over an area to "train" the algorithm by deciding a priori what end member components will be mapped within an image. These classifications allow the user to quantify the accuracy of the mapping algorithm through comparison with ground-truth data. Ultimately, we also used unsupervised classifications that do not require any knowledge of ground cover but still group and map pixels into classes based on spectral similarity. Unsupervised classifications are more subjective and exploratory, but a quantitative accuracy analysis is not possible without ground truth data. We took a hybrid approach to exploit the advantages of both methods, by mapping a small example site in the field and then using supervised classifications to find the optimum hyperspectral image data processing sequence. This allowed us to use our dataset for remote geologic mapping via unsupervised classifications over a much larger area.

The thermal infrared wavelength range, λ = 8-15 μm, is appropriate for mapping volcanic lithologies, such as those along the Lavic Lake fault, due to a silica absorption feature known as the Reststrahlen band. The Reststrahlen band appears as a minimum in emissivity spectra for silicate rocks and minerals and shifts to longer wavelengths as the

degree of silica polymerization in a rock or mineral decreases (Launer, 1952). The base unit in silicate minerals is the silica tetrahedron (SiO_4). Polymerization occurs as silica tetrahedra in a crystal structure share an increasing number of oxygen ions, which increases the Si:O ratio and resultant weight percent silica. The Reststrahlen band is positioned at a longer wavelength for olivine (found in basaltic or ultramafic rocks), a silicate mineral that lacks Si:O polymerization, than for quartz (found in rhyolite or granite), in which polymerization and resultant weight percent silica is maximized. Since differences in volcanic lithology are defined by variations in weight percent silica (e.g., Le Bas et al., 1986), the shift in the Reststrahlen band can be used to map geochemical variation in volcanic rocks (Hook et al., 2005). Therefore, spectra measured in the thermal infrared are ideal for categorizing and mapping the volcanic lithologies present along the Lavic Lake fault.

Our goal in mapping the geology and total tectonic offset of the Lavic Lake fault is to expand and improve the information relevant to active tectonics and related seismic hazards in southern California. The fault is located in the Bullion Mountains of the Mojave Desert, California, but there is limited information on the geology of this area. The long-term cumulative offset along the Lavic Lake fault is not well resolved; in older maps, the Lavic Lake fault had not been formally named, the sense of displacement was unknown, and much of the fault's surface trace was only mapped as an approximate location (Kupfer and Bassett, 1962; Dibblee, 1966 (republished in 2008); Dibblee, 1967a; 1967b; 1967c).

The 1999 earthquake and surface rupture provided key new information about this fault and also motivated additional studies. Treiman et al. (2002) were able to map the surface trace and determine that the fault slip was generally right lateral. The Hector Mine Earthquake Geologic Working Group (1999) formally named the fault after the Lavic Lake

playa, a geographic feature crossed by the northern end of the fault (Figure 2A). A cumulative offset measurement for the Lavic Lake fault was then determined via geophysical methods: Jachens et al. (2002) estimated 3.4 ± 0.8 km of dextral offset from offset magnetic anomaly pairs within the Bullion Mountains. Because the age of these offset magnetic anomaly pairs is unknown, a geologic slip rate could not be calculated. The geologic slip rate would be useful because of the discrepancy between integrated geologic fault slip rates and current geodetic crustal motion (~6 and 12 mm/yr, respectively) in eastern California (Oskin et al., 2008). Long-term average geologic slip rates for the eastern California shear zone (ECSZ) range from 8.3 ± 1 mm/yr since 12 Ma (McQuarrie and Wernicke, 2005), to ≤6.2 ± 1.9 mm/yr since ~750 ka (Oskin et al., 2008). While Oskin et al. (2008) refer to their value as "geologic" rate, it could instead be considered a "geomorphic" rate, since it is averaged over a time interval of 10^3-10^6 years (e.g, see Table 2 in Friedrich et al. (2003), where "geologic" rates are defined as averages over 10^6-10^7 years). The discrepancy between geologic and geodetic slip rates in the eastern California shear zone could be minimized by including more accurate active fault slip rates into the total.

Paleoseismology on the Lavic Lake fault in the playa area following the 1999 earthquake also yielded several important results: the surface trace of the 1999 event had not previously ruptured for at least 7000 years, but another strand with geomorphic evidence (vegetation lineaments and uplifted basalt exposures) for recent activity ruptured sometime within the past ~1750 years (Rymer et al., 2002). Rymer et al. (2002) suggested that deformation has not yet been fully localized onto a single strand, suggesting that the Lavic Lake fault is relatively young. Since fault roughness and cumulative offset vary with age, a young fault provides an important data point for evaluating seismic hazard as a function of

fault maturity. Our objective is to measure the cumulative offset, which can be combined with bedrock ages to calculate a minimum geologic slip rate, and can also be used for palinspastic reconstructions of eastern California (e.g., McQuarrie and Wernicke, 2005).

GEOLOGIC SETTING

The Lavic Lake and Bullion faults are located in the Bullion Mountains, Mojave Desert, California. The Bullion Mountains have some 200 to 400 meters of topographic relief in bedrock outcrops. These include extrusive Tertiary and Quaternary igneous rocks, and underlying hypabyssal and intrusive lithologies of pre-Tertiary age (Kupfer and Bassett, 1962). Surficial weathering of the volcanic bedrock has resulted in alteration to abundant clay and zeolite minerals, and erosion has created Quaternary surficial deposits of colluvium and fanglomerate. In the northwest portion of the Bullion Mountains where Miocene (?) to Oligocene igneous extrusive rocks crop out, the 1999 Hector Mine earthquake surface rupture along the Lavic Lake fault (Figures 1 and 2) reached a maximum right-lateral displacement exceeding 5 m (Treiman et al., 2002). Lithologic composition ranges from andesitic to basaltic, with massive and porphyritic textures (Dibblee, 1966). Bedding is right-side up in this area, and attitudes generally strike northwest with $\leq 30°$ dip to the northeast. Many small faults are present that strike approximately northwest and show some right-lateral separation, and there are also faults that strike generally east-west, with either left-lateral or unknown sense of motion (Kupfer and Bassett, 1962). The other major named structure in the area, the Bullion fault, strikes approximately northwest and bounds the southwestern extent of the Bullion Mountains. This fault is sometimes combined with others

to define the Bullion-Rodman-Pisgah fault (e.g., Richard, 1993) with net slip estimates that range from 6.4-14.4 km (Dokka, 1983), up to 20-40 km (Garfunkel, 1974).

Immediately north of the Bullion Mountains lies the Lavic Lake playa, which is composed mainly of hard packed clay (Kupfer and Bassett, 1962) and contains decameter-scale surficial fractures and fissures that are linear and polygonal in shape. The fractures persist through multiple rainy seasons, and are likely caused by some combination of desiccation and crustal deformation (some from the 1999 Hector Mine earthquake). Farther north, the 22.5 ± 1.3 ka Pisgah basalts (Phillips, 2003) are in contact with Lavic Lake playa deposits. Paleoseismic trenching and dating of Lavic Lake playa strata (Rymer et al., 2002) show that the shallowest sediments postdate the Pisgah lavas. But because the thicknesses of these units are unknown, an interfingering contact between these two units cannot be ruled out.

The Lavic Lake fault is one of many faults comprising a tectonic province formally named the Eastern California shear zone (ECSZ) by Dokka and Travis (1990a; 1990b). Estimates for the inception age of ECSZ faulting vary widely, but some straightforward constraints come from cross-cutting field relationships. A minimum age for the onset of at least some ECSZ faulting is provided by a 3.77 ± 0.11 Ma basaltic lava that drapes over a fault scarp in the Black Mountains, near the Garlock fault (Oskin and Iriondo, 2004). Schermer et al. (1996) found that <11.7 Ma Miocene fan deposits and their older substrate are cut and displaced the same amount by component faults in the northeastern Mojave Desert with left-lateral offset. A palinspastic restoration model of mountain ranges in the southwestern United States concurs with the upper age limit of Schermer et al. (1996), finding ECSZ right-lateral displacement along faults oriented on average N25°W, since c.

12 Ma (McQuarrie and Wernicke, 2005). Several other estimates of ECSZ inception age utilize disparate methods, but all fall in the range of 5-6 Ma. Regional deformation in eastern California transitioned from extensional to right-lateral shear from 6-8 Ma (Snow and Wernicke, 2000), and this generalized right-lateral shear occurs from the Death Valley region across the Garlock fault into the northern extent of the ECSZ. Modeling the deflection of the Garlock fault suggests that right-lateral shear has deformed the region since 5.0 ± 0.4 Ma (Gan et al., 2003). Miller and Yount (2002) suggest that the proliferation of east-west striking left-lateral faults within the ECSZ controlled topography and consequently the flow direction of 5-6 Ma basaltic lavas. Woodburne (2015) couples ECSZ inception with, or possibly as a byproduct of, the opening of the Gulf of California at c. 6 Ma (Atwater, 1992; Atwater and Stock, 1998; Oskin and Stock, 2003; Bennett et al., 2015), and also cites a period of non-deposition in the Mojave Desert region until c. 6 Ma to strengthen the argument of tectonic quiescence prior to that time. Constraints for the age of inception of the ECSZ are summarized in Table 1.

In compiling the tectonic history of the ECSZ, the addition of cumulative net slip across all faults can be combined with age of inception to infer long-term geologic slip rates across the region. Earlier estimates of cumulative net slip across all right-lateral faults, striking approximately northwest, generally varied between 25-65 km (Dokka, 1983; Dokka and Travis, 1990a; Jagiello, 1991; Richard, 1993), but more recent estimates increase to about 100 km (McQuarrie and Wernicke, 2005; Bennett et al., 2016). The models used to derive net slip typically invoke clockwise rotation of fault blocks or considerable off-fault, continuous strain (Richard, 1993; McQuarrie and Wernicke, 2005), as this also can explain left-lateral slip along east-west striking faults within the ECSZ (e.g., see the model of

Luyendyk et al., 1980), although some opposing views imply counter clockwise rotation of the fault blocks bounded by right-lateral faults (Garfunkel, 1974; Dokka and Travis, 1990a). Although some groups (Golombek and Brown, 1988; Ross et al., 1989) have shown compelling paleomagnetic evidence for early Miocene clockwise rotation of some areas in the Mojave Desert, MacFadden et al. (1990a; 1990b) also pointed out that paleomagnetic results can vary locally and temporally, showing that caution is required in invoking a single generalized model of uniform rotation across the entire region.

Tallied net slips have been combined with age of inception to calculate the long-term geologic slip rate across the entire region, but results vary widely, anywhere from 3-12 mm/yr since the Early, Middle, or Late Miocene (Dokka and Travis, 1990b). A more recent and precise approach, however, involves extensive field work to find dateable offset piercing points along as many of the active faults in the region as possible, then integrating these results into a single value. Such an approach was undertaken by Oskin et al. (2008), who combined geologic slip rates from six major faults with Quaternary slip to arrive at a "sum geologic Mojave ECSZ slip rate" of $\leq 6.2 \pm 1.9$ mm/yr since ~750 ka. The inequality marker indicates that they used maximum possible offset values (and subsequent rates) for six specific faults to derive the summed rate. But in another sense, the value also represents a minimum, since data do not exist for every single active fault strand within the area of the integration, and do not account for continuous, off-fault strain (e.g., McQuarrie and Wernicke, 2005). Nonetheless, this result highlights a discrepancy between results from geology and geodesy, whose scientists often collaborate to study earthquake science and seismic hazards in southern California. With GPS tracking of tectonic motion, geodetic slip rate estimates across the ECSZ are usually >10 mm/yr (Sauber et al., 1994; Dixon et al.,

1995; Miller et al., 2001; McClusky et al., 2001; Becker et al., 2005; Spinler et al., 2010; McGill et al., 2015), much faster than the sum geologic rate from Oskin et al. (2008). Some geodetic slip rates are <10 mm/yr and more closely agree with the summed geologic rate, but they are either based on older data (Sauber et al., 1986; Savage et al., 1990), alternative methods (Peltzer et al., 2001), or are modeled with greatest effort to agree with and thus solve the discrepancy between the sum geologic rate (e.g. Chuang and Johnson, 2011). Meade and Hager (2005), Oskin et al. (2008), and Spinler et al. (2010) have all pointed out that although there may have been a post-seismic flare-up following the 1992 Landers and 1999 Hector Mine earthquakes, this does not explain the discrepancy, because a relatively fast geodetic rate (Sauber et al., 1994) had already been observed prior to those two major events. Another explanation for the discrepancy is the incorporation of off-fault deformation into either the sum geologic rate, the geodetic model used, or both. In this case much of the shear strain in the ECSZ could be distributed over the entire region and not confined to the fault segments portrayed in models. Analyses that considered off-fault deformation have minimized the discrepancy significantly (e.g., McQuarrie and Wernicke, 2005; Bird, 2009; Shelef and Oskin, 2010; Johnson, 2013). The assumption that some of the fault slip is absorbed by distributed shear (i.e., off fault deformation) increases the geologic rate (e.g., Chuang and Johnson, 2011). Analogously, designing the geodetic data inversion model to incorporate off-fault deformation decreases the geodetic rate (Herbert et al., 2014). In the end, both approaches minimize the discrepancy. Even with these approaches, though, a discrepancy of a few mm/yr often remains (depending on which values are compared). Therefore, there must still be more unaccounted-for active faults with geologic slip rates that should be integrated into the sum geologic slip rate, taking into account strain compatibility with the surrounding

region, before comparing with geodetic results (McQuarrie and Wernicke, 2005). The Lavic Lake fault, having the largest and most recent surface rupturing event in the ECSZ, is a good candidate to consider, making a logical starting point for this type of analysis.

METHODS

Hyperspectral data collection

Hyperspectral airborne imagery was collected on 27 August 2013 (at 11:00 am Pacific daylight savings time) using Mako, a whiskbroom-type sensor developed by The Aerospace Corporation. Mako measures emitted surface radiance in the thermal infrared at 128 bands covering wavelengths from 7.6-13.4 μm (Hall et al., 2011; Buckland et al., 2017). We used a 1.8 km wide, 11 km long swath with 2 m pixel resolution, from a flight at 12000 feet above ground level (c. 15000 feet altitude). The footprint of the swath was centered along the Lavic Lake fault and covered the 1999 maximum slip zone of the earthquake in the Bullion Mountains (Figure 2A, 2B).

Mako sensor calibration

The Mako airborne hyperspectral infrared sensor underwent radiometric and wavelength calibration. For radiometric calibration, two onboard blackbody sources were observed immediately before and after the scene was acquired. These were stabilized at different temperatures that spanned the expected radiance values of the scene. A linear

relation between the known blackbody radiance input and the digital counting output was assumed so that the sensor response could be modeled with multiplicative gain and additive offset terms. The gain and offset terms for the pre- and post-collect calibrations were then time-interpolated to match the actual collection time of the data.

The wavelength calibration was done by observing blackbody sources covered by National Institute of Standards and Technology (NIST) traceable transparent polymer films (with calibrated absorption features), and performing a least-squares fit across the full extent of the focal plane array. For more detailed descriptions of the calibration processes, see Hall et al. (2011) and Buckland et al. (2017).

Ground truth field mapping of the Red Flake site

Using a specific field site, we quantified the accuracy to which lithology along the Lavic Lake fault can be mapped with pixel-based image classifications (Figures 2B-2F, 3, and 4A). Limited access to the field site was granted by the Marine Corps Air Ground Combat Center (MCAGCC) in December 2012 and April 2014 (Figure 3A-3C). The ground truth site was c. 5000 m^2 in size, and centered at 34.586078° north, 116.288492° west. We refer to it as the "Red Flake" site after the presence of a prominent, 1-m-tall scarp of red feldspar porphyry that protrudes from the 1999 earthquake surface rupture (Figure 3C). The site was well suited for remote sensing due to the variety of geologic units that are very well exposed with little vegetative overgrowth. We identified primary mineralogy and mapped out the contacts between distinct lithologic units. The lithologic contacts between units are diffuse over a scale smaller than the hyperspectral image pixel size (2 m), making conditions

favorable for unequivocally identifying the boundaries between distinct units with remote sensing classification methods. At the Red Flake site, we identified and mapped the following four lithologic units to guide a supervised classification: 1) tuff (and tuff breccia), 2) detritus (colluvium), 3) feldspar porphyry, and 4) microcrystalline lava (Figure 4A).

While mapping the Red Flake site, hand samples were also collected for laboratory methods: x-ray diffraction (XRD) mineral identification, and laboratory thermal infrared spectroscopy. XRD was performed with a PANalytical X'Pert Pro MPD diffractometer using copper radiation and an X'Celerator strip detector in theta 2-theta mode. Thermal infrared laboratory spectra were taken from the upward-facing weathered surfaces of the sample chips using the biconical reflectance method. Reflectance spectra were measured using a Thermo-Nicolet 6700 FTIR Spectrometer, with a Harrick Scientific "Praying Mantis" diffuse reflection accessory. All laboratory spectra were measured with a spot size of 1-2 mm, and each final spectrum was an average of 150 scans taken over 4-6 minutes. The laboratory spectra were converted to emissivity using Kirchhoff's law (Robitaille, 2009) and are shown in Figure 5. Although Kirchhoff's law cannot be used to convert biconical reflectance spectra to emissivity for quantitative purposes (Salisbury and Walter, 1989; Christensen and Harrison, 1993; Salisbury et al., 1994), the same qualitative shape results when compared to direct spectral emissivity measurements (e.g., Figure 3b in Christensen and Harrison, 1993; Figure 4 in Christensen et al., 2000).

Supervised classification of the Red Flake site

We developed the following image processing sequence to create a final supervised classification with the highest possible accuracy (Figure 6, left hand path). All processing steps, unless otherwise specified, were completed using the Environment for Visualizing Images Software, version 4.8 (ENVI, Exelis Visual Information Solutions, Boulder, Colorado). We began with data cubes of airborne thermal hyperspectral imagery that had undergone radiometric and wavelength calibration, bad pixel replacement, and spectral smile removal.

In regard to the terminology used herein regarding hyperspectral image data from the Mako whiskbroom sensor, each single whisk is a single data cube, so the words "whisk" and "data cube" are used interchangeably. The spatial extent of a single whisk relative to the complete image swath can be seen in Figure 7: in the c. 100 m-scale sawtooth pattern along the side of the image swath, the point of each tooth is the boundary between two whisks (two adjacent whisks generally have a small amount of overlap). When multiple data cubes (or whisks) are concatenated, the set of combined data cubes can be called a "super cube." Although a set of combined super cubes can still be called a super cube, the full hyperspectral imagery data set presented here consists of two super cubes with different flight line azimuthal directions (to accommodate the change in strike of the Lavic Lake fault's surface trace), and when those two super cubes are combined, we call this the "complete image swath."

For the hyperspectral image data presented here, we also removed the bands that covered wavelengths from 7.6-8.4 μm because they were dominated by noise. At this point, under normal circumstances, we would concatenate as many data cubes (whisks) as necessary to cover the area of interest and carry out the subsequent processing steps in bulk;

however, this was not necessary for the Red Flake site because the extent of the area was imaged in a single whisk. Next, we performed an in-scene atmospheric compensation (ISAC algorithm from Young et al., 2002), setting the regression pixels to maximum hit, the fitting technique to normalized regression, and using for the noise equivalent spectral radiance (NESR), the median value for the data cube(s). Then, we did a principal component analysis (PCA) to identify any variance throughout the image that resulted from noise or data artifacts (Richards, 2013). A gradation through each individual data cube was present along the flight direction, producing a spurious spectral signal that we discarded in a PCA inverse transformation (Richards, 2013). Next, we converted the data from at-sensor radiance to emissivity with the emissivity normalization method (Kealy and Hook, 1993).

We then performed the supervised classification on emissivity spectra using the spectral angle mapper (SAM, described in Kruse et al., 1993). To remain objective, "end member" spectra for each class were defined by randomly choosing 2% of the pixels from each lithologic area in the geologic map and averaging their spectra (Figure 4B, 4C). For the SAM, we imposed a maximum angle threshold of 0.1 radian, leaving very few pixels unclassified. Post-classification, we used the "sieve" and "clump" functions in ENVI (i.e, replace single pixels that were classified differently from surrounding pixels) to correct for pixel classification errors due to small desert scrub or transported lithology. We repeated this procedure ten times. The ten results were tallied via error matrices (Congalton, 1991), and then used to calculate a mean and standard deviation for classification accuracy values (Tables 2 and 3). For more detailed information about supervised classifications, see Appendix: 'Background on supervised classifications and how they were applied to this work,' and 'Guide for interpreting error matrices.'

Unsupervised classification of the complete image swath

The data processing flow chart for our hyperspectral airborne image unsupervised classification is shown in Figure 6, right-hand path. For the unsupervised classification, we first concatenated the 70 data cubes (whisks) that made up the complete aerial image swath into a single super cube, and then performed the ISAC. Then, instead of performing a PCA like we did for the supervised classification, we used a minimum noise fraction (MNF) transformation (Green et al., 1988; note that it is called a "maximum noise fraction" in that paper; also, see Lee et al., 1990). The MNF transformation involves a PCA that is performed on the data set after: 1) the noise in the data is estimated (or if known, the noise can be declared); 2) any correlations between bands are removed; and 3) the data noise variance is normalized (Kruse, 1996). The resulting principal components are then ordered by decreasing signal-to-noise ratio (as opposed to decreasing variance, as in the standard PCA). MNF performed better than PCA here, possibly due to improved noise statistics when using the entire image swath versus a single data cube for supervised classifications of the Red Flake site (where PCA was used in place of MNF because the former resulted in a higher overall classification accuracy). Figure 7 shows the complete image swath of MNF components in false color.

We found that unsupervised classifications on the complete image swath worked qualitatively better when classifying the MNF components directly without inverting back to radiance and then converting to emissivity (we still discarded any components clearly dominated by noise or data artifacts). For classifying, we used the K-Means clustering

algorithm (described in Tou and Gonzalez, 1974) with a change threshold of 5%. To ensure that every pixel would be classified, we applied no value to the "maximum standard deviation from mean" and "maximum distance error" parameters. The cluster centers stabilized below our indicated change threshold after seven iterations. Finally, we used information from Dibblee (1966) to identify the lithology that each class represented, and to superimpose lithologic contact lines for a qualitative comparison with our class boundary lines.

Within our hyperspectral image footprint, Dibblee (1966) mapped twelve separate lithologic units. While we could have used Dibblee's lithologic units as "ground truth" to perform supervised classifications (like at the Red Flake site) on the complete image swath, we wanted to pursue a more objective and exploratory method for the larger area, that could potentially identify details that had not yet been discovered. Using the same number of classes (or more) as lithologic units from Dibblee (1966) would have been ideal, but as we experimented with increasing the number of classes with the K-Means classification algorithm, the product generally became more difficult to interpret. Ultimately, we settled on using six classes (Table 4). Using six classes yielded a clear distinction between the main bedrock units in the image without making our map overly detailed, to the extent that it would be impossible to generalize broadly and interpret.

RESULTS

Ground truth field mapping of the Red Flake site

A geologic map for the Red Flake site is shown in Figure 4A, and laboratory spectra for the hand samples are shown in Figure 5. The lithologic descriptions that follow are based on a combination of field identification, hand sample description, and laboratory XRD analyses. Note that the lithologic units we identified and used for these supervised classifications are from our own on-site geologic mapping, and therefore do not necessarily correlate with any specific lithologic units from the geologic maps of Dibblee (1966; 1967a; 1967b; 1967c; 2008), which will be referenced and discussed further in subsequent sections.

Tuff (and tuff breccia)

The tuff and tuff breccia are generally white- to tan-colored, containing <1 mm grains of biotite, hornblende laths, and quartz in a microcrystalline matrix of silicate ash. Additional minerals identified with XRD are plagioclase feldspar solid solutions (andesine), potassium feldspar solid solutions (sanidine and possibly microcline), zeolites (clinoptilolite), and the high-temperature quartz polymorph cristobalite (exact quantity not determined with our methods). Laboratory spectra for the tuff and tuff breccia are shown in Figure 5A.

Detritus (colluvium)

A portion of the Red Flake site is covered in a thin veneer of detrital material. We define this as a ground truth unit because in attempts at identifying lithology from an airborne platform, only the immediate surficial material can be observed and classified. The detritus is a heterogeneous mixture of volcaniclastic sand and gravel derived from proximal lithologic

units: primarily quartz and other weathering-resistant minerals with clasts ranging from <1 mm up to 2 mm in diameter, and also some larger cobbles and boulders up to 50 cm. Additional minerals identified with XRD are calcite, plagioclase feldspar solid solutions (albite and andesine), potassium feldspar solid solutions (sanidine), and cristobalite. A laboratory spectrum for the detritus is shown in Figure 5B.

Feldspar porphyry

The feldspar porphyry may be massive or banded, and has a pinkish to dark red fine-grained matrix, with 1-10 mm phenocrysts of feldspar, occasional biotite, and rare quartz. Additional minerals identified with XRD are plagioclase feldspar solid solutions (albite), potassium feldspar solid solutions (sanidine), and cristobalite. Laboratory spectra for the feldspar porphyry are shown in Figure 5C.

Microcrystalline lava

The microcrystalline lava can be massive or banded. This unit has a very dark purple to grayish-brown microcrystalline matrix with some feldspar, glass, and vesicles up to 3 mm (vesicles can be calcite-, quartz-, or zeolite-filled). Additional minerals identified with XRD are pyroxene solid solutions (augite and diopside), and plagioclase feldspar solid solutions (andesine, bytownite, and anorthite). Laboratory spectra for the microcrystalline lava are shown in Figure 5D.

Thermal infrared laboratory spectra

We can use the Reststrahlen position (minimum in an emissivity spectrum) to compare relative silica weight percent for each of the lithologies at the Red Flake site (e.g., Launer, 1952; Hook et al., 2005. Emissivity minima wavelength positions for laboratory spectra from Red Flake site lithologies descend in the following order (followed in parentheses by the average, with one standard deviation, wavelength positions from Figure 5): microcrystalline lava (9.56 ± 0.06 μm, n = 2), detritus (9.50 ± 0.00 μm, n = 1), tuff and tuff breccia (9.26 ± 0.02 μm, n = 4), and feldspar porphyry (9.17 ± 0.44 μm, n = 3). Therefore, it is likely that the silica weight percent increases in the same order for the suite of Red Flake site lithologies. This interpretation could be complicated by weathering, alteration, and/or surficial coatings (e.g. desert varnish), since the spectra were collected from the upward-facing weathered surfaces of the sample chips.

Supervised classification of the Red Flake site

The results for the ten supervised classifications we performed are shown in Figure 8. Mean and standard deviation (one sigma) accuracy percentage values (all rounded to the nearest integer), for each lithology we defined in the field, were calculated using error matrices from the ten supervised classifications we performed, each with its own randomly generated set of end member spectra (see Figure 4B for example). The ground truth in this case was our geological map from field work (Figures 2C-2F, 3, and 4). Producer's, user's and overall accuracies are tallied in error matrices and summarized in Tables 2 and 3 (also

see Appendix: 'Background on supervised classifications and how they were applied to this work,' and 'Guide for interpreting error matrices'). The statistical spread for overall accuracy of the final supervised classification analysis was 71 ± 1% (1σ, n = 10). The microcrystalline lava had the smallest difference between producer's and user's accuracies at 89 ± 3% and 86 ± 1% respectively (Table 3). This means that on average, the method correctly classified 89% of the pixels labeled microcrystalline lava on our geologic map, and 86% of the pixels classified as microcrystalline lava across the entire Red Flake site fell within our lithologic boundaries for the unit. In contrast, the detritus had the largest difference between producer's and user's accuracies, with 71 ± 24% and 19 ± 6% respectively. Again, the method correctly classified 71% of the pixels labeled detritus on our geologic map, but only 19% of the pixels classified as detritus across the entire Red Flake site fell within our lithologic boundaries for the unit. The accuracy ratings for the tuff, and feldspar porphyry were often <50%.

Unsupervised classification of the complete image swath and interpretation as a geologic map

The complete (unsupervised classification) geologic swath map is shown in Figure 9. With the unsupervised classification, our main goal was to identify features suitable for cumulative offset measurements. Thus, we were concerned with discerning the apparent contact lines between units as revealed by the classification map. To facilitate this analysis, we took into account lithologic contact lines from published geologic maps (Dibblee, 1966; 1967a; 1967b; 1967c; 2008). Note that in this section, references to the work of Dibblee include all of those publications, but the primary reference is the 1966 map. We

superimposed the lithologic contacts from Dibblee onto our classification map, to visually check by inspection whether lithologic boundaries apparent in the unsupervised classification were true. We also added Dibblee's approximate surface trace for the Lavic Lake fault because it provided a single line for annotation that approximates the highly detailed line set of the 1999 earthquake surface rupture (Treiman et al., 2002) very well. We qualitatively evaluated the unsupervised classification evaluated by visual inspection and comparison with the lithologic contacts from the Dibblee maps, so some of these results required broad generalizations and interpretation.

We used Dibblee's maps to define lithologic compositions for our unsupervised classification units, and to compare our class boundaries with the lithologic contacts. In some areas, the class boundaries we observed in our classification map correlate very well with the lithologic contacts, but in other places they did not. A lithologic contact line between a tuff breccia and a basalt correlates well with a boundary between two of the classes from our unsupervised classification map (west-central portion of zoom inset in Figure 9, Figures 10, 11, and Table 4). The unsupervised classification also produced a unique class that spatially correlated with a felsite unit (east-central portion in Figure 9). In this case, the felsite unit also forms a topographic ridge (labeled with white arrow in main part of Figure 9), and the class extends a few hundred meters to the west and south beyond the felsite contact. The mismatch in spatial correlation is probably due to erosion and transport of rocks away from the ridge, akin to accuracy issues we described previously for the detritus in the supervised classification.

We found that in general, each one of Dibblee's bounded lithologic units contained a range of our classes (Figure 9). This was also the case for the multi-lithologic Red Flake

supervised classification site, the majority of which was more broadly mapped as andesite by Dibblee. It is possible that one or more of the lithologic units at the Red Flake site are andesitic in composition, but the precise geochemical measurements required to apply that name correctly (e.g., Le Bas et al., 1986) were outside of the scope of this study. The occurrence of multiple lithologic classes from our map included within a single one of Dibblee's bounded lithologic units could be due to topography coupled with erosion and transport of lithologic material beyond the bedrock contact lines that Dibblee mapped. Similarly, each of our classes correlated with more than one of Dibblee's lithologic units throughout the maps (Table 4), but we expected this since we used fewer classes than the number of units that he mapped in our scene. In summary, our final product is limited by the extent to which bedrock is exposed at the Earth's surface and not concealed by eroded and transported detrital material.

Ground truth lithologic units from the Red Flake site that also ended up being classes in the unsupervised analysis were the tuff and tuff breccia ("tuff breccia" in the unsupervised classification), and the detritus or colluvium ("alluvium" in the unsupervised classification). Therefore, it was possible to quantify the producer's and user's accuracies in an error matrix for those lithologic classes in the unsupervised classification at the Red Flake site. The unsupervised classification error matrix for the Red flake site is in Table 5. While the producer's accuracies in this analysis were both relatively noteworthy at >70 %, the user's accuracies were both <30 %, and the overall accuracy was 60%.

DISCUSSION

Supervised classification of the Red Flake site

The Red Flake site was chosen for the supervised classification analysis because it has excellent bedrock exposure and lacks significant vegetation. In general, lithologic alteration, erosional transport, and vegetation can create mixtures of materials for larger ground sampling distances, resulting in lower accuracy ratings for supervised classification maps. The Mako thermal airborne sensor has a pixel size of 2 m, and hyperspectral resolution (Hall et al., 2011; Buckland et al., 2017), which also helped minimize problems with the error sources that could result from spectra collected over a larger pixel size. Larger pixel sizes, with their larger ground sampling distances, can inherently incorporate greater heterogeneity of materials and create more complex spectral mixtures. Hyperspectral resolution allows for greater detail in the spectral signatures of the materials, which increases the uniqueness of spectra.

For the supervised classifications presented here, some disparities exist between the producer's and the user's accuracy ratings for individual lithologies (see Table 3, and Appendix: 'Background on supervised classifications and how they were applied to this work,' and 'Guide for interpreting error matrices'). The highest disparity between accuracies found for a single lithology occurred with the detritus class. The low user's accuracy for the detritus class may be caused by transported sediment if surficial deposits of detrital material are large enough to dominate the spectra for groups of pixels that we mapped as exposed outcrop of other classes. The heterogeneity of the detritus may also contribute to its internal inconsistency in the producer's accuracy, as it is intrinsically produced by weathering, transport, and mixing of adjacent units. Geometric surface roughness and erosion to smaller

grain sizes can also suppress spectra for pure end members by reducing spectral contrast (Cooper and Mustard, 1999; Kirkland et al., 2001; Horgan et al., 2009), weakening signatures and further decreasing accuracy. Therefore, a primary conclusion from the supervised classification analysis is that the presence of detrital material (e.g., colluvium/alluvium/etc.), which is inevitable in natural settings, will lower the accuracy of lithologic classification maps.

Average values for the producer's accuracies of the tuff and tuff breccia (38 ± 16 %), and of the feldspar porphyry (34 ± 4 %), are both <50% (Table 3). The tuff is often incorrectly classified as detritus, and the feldspar porphyry is often incorrectly classified as microcrystalline lava. The incorrect classifications could be due to compositional similarity between lithologies. The average value for the user's accuracy of the tuff and tuff breccia (25 ± 5 %) is also <50%, but the feldspar porphyry has a user's accuracy (62 ± 6 %) that is nearly double its producer's accuracy. For practical applications, the user's accuracy can be a more important statistic, given that it is the probability that a material, when field-checked, will actually be what the map claims that it is (e.g., Congalton, 1991).

The performance of the microcrystalline lava is generally excellent with both producer's and user's accuracies (89 ± 3 % and 86 ± 1 %, respectively) >85%. Given the classification performance problems described above with respect to weathering, it is possible that the microcrystalline lava was classified better due to the unit being relatively less susceptible to erosion. Overall, our statistics show that out of the four lithologic units that we used as ground truth, the microcrystalline lava is probably the most dependable for classification mapping.

Lavic Lake fault piercing lines and cumulative offset

To estimate the cumulative long-term offset along the Lavic Lake fault, we needed to identify a piercing line within older bedrock units that was subsequently cut by the fault. The intersection of the piercing line with the fault then defines a piercing point, which then can be used to define the net slip. Piercing lines such as offset stream channels are often used for measuring coseismic displacement from earthquakes that occur in the present time, but such ephemeral features do not capture long-term offset that has accumulated since inception of the Lavic Lake fault. In offset bedrock units, linear geologic features are relatively rare, but the intersections between two planar features that can be confidently correlated across the fault are typically used. For example, the intersection of a lithologic contact (or specific bedding plane) with an igneous dike, the hinge surface of a fold, or a fault that clearly pre-dates the fault offset in question, are typically used. For our purposes, we looked for a lithologic contact and older fault plane that could be clearly identified on both sides of the Lavic Lake fault. This was the primary motivation for discerning the apparent boundaries between lithologic units as revealed by our classification maps. Superimposing Dibblee's (1966) lithologic contacts onto our remote sensing imagery products served as a qualitative assessment to reinforce the validity of any lithologic boundaries apparent in the unsupervised classification. As discussed below, two such intersections or piercing lines were identified that may serve as displaced features to constrain the net slip vector, which gives the magnitude of displacement.

Our analysis is based on some key observations from the geologic maps (Figures 9, 10, 11, and also see Table 4), high-resolution satellite imagery (Figure 12), and ground-based

field photographs (Figure 13). Of primary importance in the volcanic stratigraphy are a tuff breccia (Dibblee's "Tt," see Figures 9, 10, 11C, and Table 4) and a basalt (Dibblee's "Tb," see Figures 9, 10, 11C, and Table 4). Note that these units are designated and referenced from the combined analysis of our unsupervised classification with Dibblee's (1966) geologic map, rather than any similar or identically-named units from our supervised classification analysis at the Red Flake site. We determined that bedding in Tt and Tb is right-side up, based on attitudes plotted on the Dibblee map (Figure 10) for crude bed forms within these units that are apparent in the oblique view satellite imagery (Figure 12), and field photographs (Figure 13). In true color, Tt is a very light shade of tan, and Tb is an overlying, very dark brown to black shade (Figures 12 and 13). Thus, Tt is older than Tb by stratigraphic superposition.

We were interested in using the lithologic depositional contact between Tt and Tb as part of an offset piercing line, so hereafter, we refer to this feature as the "Tt/Tb contact," after the abbreviated lithologic letter codes from the Dibblee (1966) map. In our unsupervised classification map (Figure 9, see lower left zoom inset, and Figure 11B), the Tt/Tb contact is revealed as a generalized boundary between the green-color-coded "tuff breccia" (Tt) and the blue-color-coded "basalt" (Tb). With Dibblee's lithologic contacts superimposed onto our unsupervised classification (Figures 9, 10, and 11), the general designation between the tuff breccia and basalt becomes more evident (also see Figure 7), albeit somewhat obfuscated by scattered alluvium and other lithologies (i.e., weathering, erosion, and transport of the various rock types that coexist in proximity to one another). Tt and Tb strata, and their contact boundary, generally dip 15-30º east/northeast (Figure 10 and 11C). At the location where we used the maps to measured fault offset (west-central portion of zoom inset of Figure 9, and

Figures 10 and 11), a younger lithologic unit, the fanglomerate of andesitic detritus (Dibblee's "Tfa," see Figure 10 and Table 4), overlies Tb in angular unconformity. Tfa's base appears relatively flat, as indicated by the fact that its basal contact with older units follows topographic contours. This relationship between Tb and Tfa is also clearly defined on Dibblee's map at a location some 5 km west of the location shown in Figure 10.

Another younger lithologic unit overlies the volcanic bedrock (including Tt, Tb, and their depositional contact) in angular unconformity, a rhyolitic felsite (Dibblee's "QTr," see Table 4). QTr's base also appears relatively flat, because its basal contact also follows topographic contours. Note that QTr is not the same lithology as the felsite class shown in Figure 9; that felsite is correlated with an intrusive felsite (Dibblee's "Tif," see Table 4). One bedrock exposure labeled "QTr" in Dibblee's maps is now known to be Peach Spring Tuff (Wells and Hillhouse, 1989), which has implications for age control on aspects of the system we are considering here. The age of the Peach Spring Tuff is 18.78 ± 0.02 Ma (Ferguson et al., 2013). ECSZ age of inception is generally considered to be 5-10 Ma (Table 1), much younger than the Peach Spring Tuff. Thus, the Peach Spring Tuff is older than the ECSZ and the Lavic Lake fault. Therefore, we are confident that the Tt/Tb depositional contact pre-dated inception of the Lavic Lake fault, so using the contact as a component plane of our piercing line captures the complete offset of the Lavic Lake fault.

Displaced Tt/Tb contact: the vertical component of slip

On the west side of the main Lavic Lake fault, the Tt/Tb contact appears in our remote sensing maps (Figures 7, 9, and 11), Dibblee's mapped lithologic contacts (Figure 10), and

also an additional published geologic map (Kupfer and Bassett, 1962). Although the displaced Tt/Tb contact has apparent right-lateral map-view separation in Dibblee's map (Figure 10), because the contact is a planar geologic feature, it cannot, as a matter of definition, be used as an offset feature to measure net slip across the Lavic Lake fault. On the west side of the main Lavic Lake fault, Dibblee's Tt/Tb contact is depicted as depositional, but we discovered by using our ground-based field photographs and satellite imagery, that the contact line is actually a separate and distinct, smaller cross fault where the feature intersects the main fault (Figures 12 and 13). On the east side of the main fault, the Tt/Tb contact is also depositional, but does not clearly align with a distinct class boundary from our remote sensing map (Figure 9, southeast portion of the zoom inset, and Figure 11). This is partly because the Tt/Tb contact does not intersect the main fault on its east side, as depicted in Dibblee's map (Figure 10); instead, the contact is truncated by a separate and distinct, smaller cross fault. The smaller cross fault that truncates the Tt/Tb contact on the east side of the Lavic Lake fault is apparent in satellite imagery (Figure 12). The southernmost portion of the area mapped as Tt along the Lavic Lake fault on Dibblee's map (Figure 10) is mapped as basalt on another published geologic map, and shown in fault contact with Tt (Kupfer and Bassett, 1962). Figure 12 shows Dibblee's depiction of the Tt/Tb contact compared to our depiction of the same feature. In Figure 12B, Dibblee's Tt/Tb contact is depicted as wholly depositional, except where the two lithologic units are in fault contact along the main fault. Figure 12C shows our observations of the smaller additional structures that exist in relation to the Tt/Tb contact and the main fault. On the west side of the main fault, the contact is partly depositional and partly fault. On the east, the depositional contact is truncated by a distinct, smaller cross fault.

As noted above, the apparent horizontal separation of a planar feature is insufficient to indicate the true displacement vector of net fault slip. The separation of a stratigraphic plane, versus true net slip, is a classic problem in structural geology, because a linear feature can appear to have been tectonically displaced in a specific way when viewed in a two dimensional perspective (such as an overhead map view), but the three dimensional consideration shows that a given separation can result from a wide variation in net slip. For example, a dipping stratum can appear to be offset laterally by a fault in map view, but the observed separation can actually result from pure dip-slip (e.g., Figure 8.6 in Fossen, 2010; Figure 6.48 in Davis et al., 2012). The variety of possible spatial orientations and intersections between strata, contact boundaries, and fault planes will inevitably create ambiguity when considering separation versus slip.

Bedding attitudes given in the Dibblee maps show that the strike of Tt and Tb bedding (and by extension, their depositional contact) is fairly consistent in proximity to the main Lavic Lake fault (Figure 10). The angle of intersection between bedding and the fault is about 70 to 75°, and the map-view trace of the Tt/Tb depositional contact is mainly subparallel to the trend of the main fault trace (Figure 10). The subparallel geometry between the Tt/Tb contact trace and the main fault trace would lead to significant error if considering horizontal map-view separation of the contact versus true fault slip. The very low angle of intersection between the Tt/Tb depositional contact trace and the fault trace contributes to an exaggerated amount of perceived lateral separation, and the cross section that traverses the main fault at this location (line A-A' in Figure 10) shows that the Tt/Tb depositional contact has apparent vertical separation. The cross section reveals a solution that invokes a purely vertical offset of the Tt/Tb contact, but the map-view separation allows a purely horizontal

strike-slip offset also, depending on the dip direction of the contact prior to offset. The topographic relief and broad surface elevation are greater on the east side of the main Lavic Lake fault than on the west side, which we interpret to represent a component of cumulative and significant pre-1999 vertical fault displacement, with the east block upthrown relative to the west block (cross section A-A' in Figure 10).

The apparent vertical separation that we measured in the cross section (Figure 10) is 240 m. We derived an error range for that measurement by considering variability in the cross-section-projected dip of the Tt/Tb contact, and also a relatively small amount of variability in the dip of the main Lavic Lake fault (as described below). Average cross-section-projected dip domains on the west and east side of the Lavic Lake fault are 13º and 23º (both east/northeast), respectively, and this variation in dip affects the vertical separation estimate. We also considered variation in the dip of the Lavic Lake fault itself. Geodetic inversion models show that some portions of the Lavic Lake fault dip 75-90º east/northeast (Simons et al., 2002). With all of the data combined, we calculated the minimum apparent vertical separation by assuming that the Tt/Tb depositional contact had minimum cross-section-projected dip on both sides of the fault (13º east/northeast), and the fault had maximum dip (90º). We calculated the maximum by assuming that the contact had maximum cross-section-projected dip (23º east/northeast) and the fault had minimum dip (75º east/northeast). We derived the intermediate value by assuming the average cross-section-projected dip domains for the west and east sides of the main fault (13º and 23º, respectively), and that the fault had a 90º dip. The value for apparent vertical separation is: minimum 210 m, intermediate 240 m, and maximum 370 m, or 240 +130/-30 m.

We note that on the basis of the apparent vertical separation of the Tt/Tb contact alone, the vertical component of net slip cannot be resolved. For example, if the contact dipped northeast prior to faulting, then purely left-lateral net slip would produce a vertical separation of the contact with the east side upthrown. However, at the location in discussion, the strike of bedding in Tt/Tb is nearly parallel to the fault trace, or said in another way, the dip direction of the Tt/Tb contact is very close to perpendicular to the fault trace (Figure 10). With the very small acute angle (5-10º) between bedding strike and the trace of the Lavic Lake fault (Figure 10), left-lateral slip of at least a few kilometers would be required to produce the apparent vertical separation of 240 m. Left-lateral slip in that amount is very large and, and in the wrong sense of the coseismic slip of the 1999 earthquake. Furthermore, for any area where the fault trace and bedding strike are parallel, no amount of strike slip in either direction can produce a net vertical separation of the contact. If we assume that, like all of the other major northwest trending faults in the ECSZ, the Lavic Lake fault has net slip that is mainly right-lateral strike slip, then the vertical separation is probably the result of a true component of vertical slip. Thus, we interpreted the apparent vertical separation as the vertical component of the slip vector, which we then combined with a horizontal component, to solve for the magnitude of displacement.

Displaced cross fault: the horizontal component of slip

As stated previously, much of the Tt/Tb contact trace is depositional, but west of the main fault, the Tt/Tb contact intersects the main fault as a separate and distinct, smaller cross fault (Figures 12C and 13). In proximity to the main fault, on its west side, the Tt/Tb contact

trends along a 5-10º azimuth. However, at a point c. 200 m from the main fault trace, the contact line makes an abrupt 120º turn immediately before intersecting the main fault trace. There is not actually an abrupt change in azimuth along the Tt/Tb depositional contact right before it intersects the main fault; instead, we attribute the sudden and drastic change in azimuth to the smaller cross fault. The Tt/Tb fault contact here is further evidenced by the structural juxtaposition of older Tt on top of younger Tb. Figure 13B and 13D shows ground-based field photographs where this portion of the Tt/Tb contact is a smaller cross fault, as evidenced by how the older, light-hued Tt strikes at high-angle into, and structurally overlies, the younger, dark-hued Tb. While we interpreted this field relationship as a fault contact, we note the possibility that the Tt and Tb units interfinger with one another, as implied by Dibblee's interpretation, and by Kupfer and Bassett (1962).

On the east side of the Lavic Lake fault, the Tt/Tb depositional contact does not intersect the main fault as shown by Dibblee (southern center portion of Figure 10, Figure 11), because as noted above it is cut by a separate and distinct, smaller cross fault (Figure 12C; Kupfer and Bassett, 1962). The cross fault that truncates the Tt/Tb contact on the east side of the main fault could be the same fault as the cross fault on the west. This correlation is strengthened by the fact that both cross faults have a separation that is downthrown to the south, juxtaposing the younger basalt on the south side with the older tuff on the north side. If the two cross faults on each side of the main fault are indeed the same (that is, an older fault that pre-dates inception of the Lavic Lake fault) then the older cross fault has been cut and displaced by the main fault, and the older cross fault's surface trace defines a feature that is independent of offset of the Tt/Tb contact. Because the fault trace strikes at a high angle to the Lavic Lake fault, if it has a steep dip (see below), then its offset serves as a fairly

accurate estimate of horizontal displacement. Any purely dip slip solution for the net slip vector would require many kilometers of vertical displacement, which would violate the modest vertical separation defined by the shallowly dipping Tt/Tb contact. We therefore interpret the map-view lateral separation of the cross fault as an accurate estimate of the horizontal component of slip along the Lavic Lake fault.

The apparent map-view right-lateral separation of the cross fault by the main Lavic Lake fault is 930 m, and we estimate an error of ±30 m based on possible variation of its precise intersection lines with the main fault. The cross fault on the east appears to have steep dip, based on its relatively straight surface trace. The cross fault on the west, though, could have a low dip angle, as suggested by its highly meandering surface trace (Figure 12C). While it is possible that the cross faults are not correlative (which would completely invalidate the horizontal separation measurement), tectonic deformation by the main fault could have resulted in different dip angles for the cross fault's displaced, complementary components. But if the cross fault originally had, or does have a shallow dip, then we again encounter the nonuniqueness in the separation versus slip problem, where a small amount of vertical fault motion along the main fault could have produced significant apparent lateral separation of the cross fault's surface trace. We do not have any subsurface or other data to determine if the cross fault has a low dip, but we can assign the horizontal separation as a maximum value, where less total slip can be inferred to the extent that the fault dip is very shallow.

Slip vector and off-fault deformation

We used our estimates of the horizontal and vertical separation components (both at the same location) to estimate a total slip vector and solve for the magnitude of displacement. The vertical separation of the Tt/Tb contact is 240 +130/-30 m down on the west, and the horizontal separation of the cross fault is 930 ± 30 m right-lateral. By the Pythagorean theorem, we therefore estimate the net slip to be 960 +70/-40 m (error range from solving for the maximum/minimum vertical and horizontal values).

We assumed that the Lavic Lake fault as a whole has predominantly experienced strike-slip displacement since its inception, similar to other components of the ECSZ that have locally large components of dip slip (e.g., Spotila and Sieh, 1993), and concluded that the slip vector and displacement magnitude presented here represent the cumulative long-term offset of bedrock. Unresolvable uncertainties remain regarding prehistoric slip on the main fault (e.g., lateral/strike slip versus dip slip) and structural geometry of the cross fault (e.g., the dip angle), so we consider the cumulative offset value presented here to be a maximum (since ECSZ inception at 5-10 Ma, see above, and Table 1). Our value of <1 km is significantly less than the magnetic gradient offset estimate of 3.4 ± 0.8 km (Jachens et al., 2002), but our measurement is from a different location that is 3-5 km away to the north from theirs. We are confident that we captured the entire cumulative offset recorded at the surface by the Lavic Lake fault, because the Lavic Lake fault is younger than the piercing lines (Tt/Tb contact is >18.78 ± 0.02 Ma from overlying QTr = Peach Spring Tuff, see above) that we used to derive the slip vector. The difference between our surface measurement and the magnetic measurement, then, may be due to factors of 3D basement geometry, as well as off-fault continuous deformation, or tectonic displacement along discrete, smaller adjacent structures.

Off-fault deformation has been cited as a potentially significant source of error in considering the discrepancy between long-term geologic and current geodetic slip rates (Bird, 2009; Shelef and Oskin, 2010; Chuang and Johnson, 2011; Johnson, 2013; Herbert et al., 2014). Off-fault continuous deformation is more likely to occur in unconsolidated sediments (e.g., the Lavic Lake playa to the northwest, or alluvium to the southeast), than in the bedrock where we performed a cumulative slip analysis. In alluvium to the southeast of the cumulative offset area presented in this study, Treiman et al. (2002) observed off-fault continuous deformation: 7 cm of right-lateral offset in a 7-m wide zone. Smaller, discrete adjacent faults can also contribute to off-fault deformation. For example, in the southernmost portion of the 1999 earthquake surface rupture, where offset was recorded along three distinct fault traces, up to ~2 m of fault-parallel lateral displacement was recorded in the field on secondary structures (Figure 3 in Treiman et al., 2002).

While the cumulative long-term offset along smaller faults are unlikely to be as large as that of the main Lavic Lake fault, if there are a number of these smaller faults, their integrated displacements could be significant. However, the uncertainties associated with smaller, ambiguous structures might be so high as to render such measurements meaningless. Also, it is possible that considering increasingly smaller features with increasingly smaller displacements would yield diminishing returns, akin to the Gutenberg-Richter Law, which shows the contribution of smaller earthquakes to cumulative seismic moment. For all of the reasons cited above, it is unlikely that off-fault deformation contributes significantly to the cumulative offset measurement presented here for the Lavic Lake fault.

Relative merits of the remote sensing methods used in this study

The supervised classifications we did were at a location (the Red Flake site) distant from the cumulative fault offset analysis area, but the supervision process helped us accomplish the goals in this study by allowing us to experiment with the processing sequence for quantifying and maximizing lithologic mapping accuracy values. The supervised classification overall accuracy was maximized at 71 ± 1%, by classifying the bands with wavelengths from 8.4-13.1 μm, on the emissivity data product. However, we also attempted supervised classifications on other products of the same data, including with atmospheric compensation only, the PCA components, the MNF components, and subsets of bands from those data products. The supervision process did not directly contribute to the cumulative fault offset analysis, but due to the limited access to the area for field work, experimenting with the processing sequence gave us experience and knowledge about how effectively we could differentiate some of the volcanic rocks in the area with remote sensing data and methods. We could have gone on to attempt supervised classifications of the complete image swath, using lithologic identifications and contact line work from the Dibblee (1966) map as ground truth. However, we chose to instead perform unsupervised classifications on the complete image swath because we were interested in using a more exploratory method that had the potential to highlight any features that had not been previously discovered, and could potentially assist in our cumulative fault offset analysis. Still, including the supervision process (if possible) could be an integral component to future studies that use remote sensing for geologic mapping.

In mapping the lithology along the complete image swath, we could have also opted to use the MNF false color image in a similar way to how we used the unsupervised

classification image to visually and qualitatively compare class boundaries with Dibblee's (1966) contact line work. The MNF image (Figure 7) is based on a continuous spectrum of false color to depict lithologic variation, whereas the unsupervised image (Figure 9) is based on discrete colors to represent a finite number of lithologic classes. With a finite number of discrete color assignments, the unsupervised classification method had the potential to simplify and clean up the MNF image by categorizing and sorting all of the lithologic material into a smaller set of units, which could assist in image interpretation for a more effective and synoptic summary.

Figure 11 shows a side-by-side comparison of the cumulative fault offset analysis area that we focused on for this study: the MNF components in false color (Figure 7), the unsupervised classification (Figure 9), and a portion of the Dibblee (1966) map (Figure 10). While each of the images has its own individual merits, it would not have been possible to accomplish the goals of this study without each of the three images used together. In the MNF components image, the Tt/Tb depositional contact is clearly visible on the west side of the Lavic Lake fault by a boundary between false color assignments. This boundary aligns almost perfectly with Dibblee's contact line from the 1966 map, and the lithologic descriptions from the 1966 map provided information about what type of rocks these are. However, the Tt/Tb depositional contact on the east side of the Lavic Lake fault, while depicted to be very straight forward in Dibblee's map, is not readily apparent in the MNF image. As stated above, performing the unsupervised classification provided an opportunity to simplify the MNF image into a data product that would be more straight forward to interpret. Since the unsupervised image did not yield that desired result in this case, the MNF image was optimal for the purposes of this study. In general, though, it is ideal to experiment

with and incorporate as many of the data products as possible (e.g., to see where they might agree/disagree with each other, and reveal/obscure features) into a more conclusive summary. This is why we also used the data from the Kupfer and Bassett (1962) map, which depicts the cross fault on the east side of the Lavic Lake fault. We verified the location of the east cross fault using true color Google Earth satellite imagery (Figure 12C), and went on to discover that the east cross fault is possibly correlative to the west cross fault that we verified from our field data (Figure 13), and therefore could be used as a cumulative offset marker along the Lavic Lake fault.

Implications for estimates of slip rate on the Lavic Lake fault

In regard to the discrepancy between ECSZ geologic (~6 mm/yr) and current geodetic (>10 mm/yr) slip rates, the c. 1 km cumulative displacement that we calculated is relatively small, and would not make a significant contribution to minimizing the difference. As noted above, the summed geologic ECSZ slip rate (based on six major faults across the Mojave Desert with Quaternary slip) is $\leq 6.2 \pm 1.9$ mm/yr since ~750 ka (Oskin et al., 2008), and most geodetic studies find an overall contemporary slip rate of >10 mm/yr (Sauber et al., 1994; Dixon et al., 1995; Miller et al., 2001; McClusky et al., 2001; Becker et al., 2005; Spinler et al., 2010). One of the more recent publications even cited a geodetic value of >15 mm/yr (McGill et al., 2015). The Lavic Lake fault would require a geologic slip rate of at least 4 mm/yr (i.e., bring the ~6 mm/yr total up to ~10 mm/yr) to make a significant contribution in minimizing the difference. With a slip rate hypothesized or determined, and the cumulative offset known from this study, the age of inception of the Lavic Lake fault can

be calculated. A 4 mm/yr slip rate with 1 km of cumulative offset suggests that inception of the Lavic Lake fault occurred c. 250 ka. Most of the research suggests that the ECSZ age of inception is >5 Ma (Table 1), so if the 4 mm/yr slip rate is correct, the Lavic Lake fault is a very young structure in the overall ECSZ architecture. Paleoseismological studies in the Lavic Lake playa area after the 1999 earthquake suggest that the Lavic Lake fault is a relatively young structure, with deformation that has not yet been fully localized onto a single strand (Rymer et al., 2002). A separate, proximal strand of the Lavic Lake fault that did not rupture in 1999 had ruptured within the past c. 1750 years (Rymer et al., 2002). If earthquakes occurred once every 1750 years for 250,000 years, each event with 5 m of slip, only c. 700 m of slip would accumulate (i.e., somewhat less than our estimate of c. 1 km).

If tectonic motion along the Lavic Lake fault initiated much earlier, though, for example at 1 Ma, then the geologic slip rate (using 1 km cumulative offset) would be 1 mm/yr. A 1 mm/yr slip rate for the Lavic Lake fault would be too low to significantly minimize the difference between geologic and geodetic slip rates. Furthermore, the Lavic Lake fault appears to be one of the few remaining major faults whose geologic slip rate is unknown and needs to be integrated into the summed geologic Mojave ECSZ rate. As this study on analyzing the geologic slip rate for an additional major structure in the ECSZ suggests, it seems unlikely that the discrepancy between geologic and geodetic slip rates can be resolved by simply finding and analyzing more faults for geologic slip rates to integrate.

Geologic slip rates are often minimum values, because of uncertainty in the time lag between the age of the displaced feature and inception of fault motion. Assuming this error source manifests consistently, that in itself could explain the discrepancy, because the true geologic rate would be larger than any value calculated with available methods. On the other

hand, if the geologic rates are accurate and the discrepancy really does exist, perhaps the ECSZ is currently experiencing some type of transient, or permanent, accelerated deformation rate.

CONCLUSIONS

Thermal hyperspectral airborne imagery and remote sensing techniques greatly supplemented our geologic field mapping within a restricted area along the Hector Mine earthquake surface rupture in the eastern Mojave Desert. We could not conduct an extended campaign for detailed field mapping along the entire Lavic Lake fault, but with supervised classifications over a small test site, we processed the remote sensing data to maximize accuracy in lithologic classification mapping of the volcanic rocks in the area. We also compared an unsupervised classification over the complete aerial image swath with a published geologic map of the same area. This served as a qualitative accuracy check for both the unsupervised classification map and the published geologic map. We were able to map generally the same variation and distribution of lithology with classification errors occurring mainly due to erosion and transport of heterogeneous detrital material, and possibly because the materials were similar in composition.

We used available geologic maps, along with satellite imagery, and field work to identify and measure the separations of planar features by the Lavic Lake fault. Some of the class boundaries in our remote sensing map displayed compelling correlation with lithologic contacts that were previously mapped. A mapped lithologic contact between a tuff breccia (Tt) and a basalt (Tb) correlated well with a boundary between two of the classes from our

remote sensing map. This Tt/Tb contact is cross cut and displaced by the Lavic Lake fault, with a vertical separation of 240 +130/-30 m. On the west side of the main Lavic Lake fault, the Tt/Tb contact intersects the main fault as a separate, smaller cross fault, and on the east side, the depositional contact is truncated by another separate, smaller cross fault. The right-lateral horizontal separation of this cross fault by the main Lavic Lake fault is 930 ± 30 m.

Neither the apparent vertical or horizontal separation measurements individually represent the cumulative slip along the Lavic Lake fault, but they occur at the same location, so we used them to construct the complete slip vector and calculate the magnitude of displacement. The magnitude of displacement is 960 +70/-40 m. This value is an upper limit, since some uncertainty exists regarding prehistoric slip and structural geometry. However, the magnitude of displacement that we calculate is much less than another independent cumulative offset estimate (~3 km) that was based on an offset magnetic gradient. The geologic features that we used to estimate the slip vector pre-date inception of the main Lavic Lake fault, so we are confident that the magnitude of displacement is the cumulative long-term offset of bedrock, expressed at the surface, along the main fault, since 18-19 Ma. The difference between our surface measurement and the magnetic measurement might be due to 3D basement geometry, as well as off-fault deformation accommodated by continuous strain or other smaller, discrete structures adjacent to the fault.

The magnitude of displacement that we calculate can assist in reconstructing fault histories in eastern California, and can be combined with bedrock ages to calculate the geologic slip rate. Fortunately, with its remote and inaccessible location, the Lavic Lake fault does not currently pose a major threat to society and infrastructure. Calculation of a geologic slip rate for the Lavic Lake fault may help in resolving the discrepancy between current

geodetically measured tectonic motion and integrated geologic slip rates over faults across eastern California, but based on the relatively small cumulative long-term slip that we infer, it does not appear that the Lavic Lake fault will contribute significantly to the sum geologic Mojave ECSZ slip rate.

ACKNOWLEDGEMENTS

This material is based upon work supported by the National Science Foundation (NSF) Graduate Research Fellowship Program under Grant No. 1144469 awarded to R. Witkosky, and also by Southern California Earthquake Center (SCEC) Award No. 14160 awarded to J. Stock This paper is SCEC Contribution No. 8898. SCEC is funded by NSF Cooperative Agreements EAR-1033462 & EAR-0529922, and United States Geological Survey Cooperative Agreements G12AC20038 & 07HQAG0008. Mako airborne hyperspectral imagery was acquired under the auspices of the Aerospace Corporation's Independent Research and Development program. We thank the Marine Corps Air Ground Combat Center in Twentynine Palms, California, for allowing access to the military base. We also thank Ken Hudnut, Janet Harvey, Kate Scharer, and Sinan Akçiz for their help and support in field work, performing this research, and preparing this manuscript.

APPENDIX

Background on supervised classifications and how they were applied to this work

After compiling our ground-truth data into a geologic map, we used this information to perform supervised classifications on the portion of the hyperspectral imagery that covers the Red Flake site. A supervised classification is a common remote sensing product where pixels in an image are organized into a set of classes defined a priori by a user who has knowledge of materials or land cover present in the image. In defining the classes, a few pixels are chosen to represent each class as "end members." Then, the other pixels in the image are each grouped with the end member with whom it shares the greatest spectral similarity. For our case, the classes are the four main lithologic units that we observed in the field.

After pixels are organized into classes, physical boundaries between classes are superimposed on the image in order to determine how many pixels in each area were assigned to their correct class. Results for correctly and incorrectly identified pixels are tabulated and offer a quantitative summary—as the percentage of pixels mapped correctly in relation to ground truth—for the accuracy to which the classes can be mapped using a remote sensing data set. For our purpose, the supervised classification was a test to establish how well spectral information embedded within the thermal airborne imagery allowed for differentiation of distinct lithologic units on the scale of the pixel size.

For further clarity, we present an example case: a lithologic unit is observed and its boundary mapped in the field. A remote sensing image completely covers the map view extent of this unit, so the lithologic boundary is digitized and superimposed on the image. Spectra from a few pixels within the boundary are chosen to represent the lithologic unit. In an ideal supervised classification, all of the other pixels within the boundary should be grouped, based on spectral similarity, with the chosen representative pixels. In the real world.

However, complications exist that make a 100% accuracy rating for a supervised classification highly unlikely. Compositional heterogeneity of surficial material due to alteration, vegetation, transport, and/or incomplete knowledge often results in mixtures of materials for each pixel. Geometric surface complexity (intrinsic roughness and/or erosion to small angular grains) can also complicate spectra for pure end members by reducing spectral contrast, resulting in weak signatures (Cooper and Mustard, 1999; Kirkland et al., 2001; Horgan et al., 2009). Nonetheless, our choice of sensor and site minimized these problems. The Mako sensor has a pixel size of 2 m, with hyperspectral resolution (Hall et al., 2011; Buckland et al., 2017), and the Red Flake site offers excellent bedrock exposure with a lack of significant erosion or vegetation.

The spectral angle mapping algorithm (SAM, described in Kruse et al., 1993) calculates the n-dimensional angle, where n is the number of bands, between the spectrum for each pixel and the spectrum for each end member using the geometric definition of an inner product. Each pixel is then classified as the end member for which the minimum angle is calculated. Finally, lithologic contacts from our geologic map were superimposed to assist in visualizing the classification accuracy, and we assessed the accuracy of the supervised classification via error matrices (Congalton, 1991). Figure 8 shows the results for the ten supervised classifications (labeled A through J), and the corresponding error matrices are in Table 2.

Guide for interpreting error matrices

Here we provide a detailed explanation, with examples, for how to interpret error matrices and calculate producer's, user's, and overall accuracies. All of the following explanations reference numerical values in the error matrix from supervised classification A (see Figure 8 and Table 2).

Reading down a column of the error matrix shows the distribution of classified pixels within each ground truth class. For example, the first column shows that in the bounded region that we mapped as tuff, 25 pixels were correctly classified as tuff, but 11, 13, and 13 pixels were incorrectly classified as detritus, feldspar porphyry, and microcrystalline lava, respectively. Thus, summing over a column gives the total number of pixels contained in each bounded ground truth area. The total number of pixels classified correctly as a fraction of the total number of pixels in a column gives the "Producer's accuracy." The name is in reference to a scenario where the producer of the classification map wishes to assign a grade to their product, so they simply quantify how many pixels are correct in each bounded class area. For the tuff, this is 25/62 = 0.40 or 40%.

Reading across a row of the error matrix shows how many pixels for each type of lithology were classified into each ground truth class. For example, the first row shows that 25 true tuff pixels were correctly classified as tuff, but 2 true detritus, 56 true feldspar porphyry, and 4 true microcrystalline lava pixels were incorrectly classified as tuff. Thus, summing over a row gives the total number of pixels classified as a given lithology throughout the entire classification map. The total number of pixels classified correctly as a fraction of the total number of pixels in a row gives the "User's accuracy." The name is in reference to a scenario where a user of the classification map field-checks every pixel and

then assigns a grade based on misclassified pixels across the entire scene, not just grading within the individual class boundaries. For the tuff, this is 25/87 = 0.29 or 29%.

Taking the sum of the diagonal of the error matrix gives the total number of pixels classified correctly in relation to ground truth. The total number of pixels classified correctly across all classes, as a fraction of the total number of pixels in the classification map gives the "Overall accuracy," which is the lowest entry to the right. For supervised classification A and its accompanying error matrix, this is 25 + 28 + 125 + 747 = 925, then 925/1297 = 0.71 or 71%.

REFERENCES CITED

Arrowsmith, J.R., and Rhodes, D.D., 1994, Original Forms and Initial Modifications of the Galway Lake Road Scarp Formed along the Emerson Fault during the 28 June 1992 Landers, California, Earthquake: Bulletin of the Seismological Society of America, v. 84, n. 3, pp. 511-527.

Atwater, T., 1992, Constraints from plate reconstructions for Cenozoic tectonic regimes of southern and eastern California, *in* Richards, S.M., ed., Deformation associated with the Neogene Eastern California Shear Zone, southwestern Arizona and southeastern California: San Bernardino County Museum Special Publication, v. 92-1, p. 1-2.

Atwater, T., and Stock, J., 1998, Pacific-North American plate tectonics of the Neogene Southwestern United States: An update: International Geology Review, v. 40, p. 375-402, doi:10.1080/00206819809465216.

Becker, T.W., Hardebeck, J.L., and Anderson, G., 2005, Constraints on fault slip rates of the southern California plate boundary from GPS velocity and stress inversions: Geophysical Journal International, v. 160, p. 634-650, doi: 10.1111/j.1365-246X.2004.02528.x.

Bennett, S.E.K., Oskin, M.E., Dorsey, R.J., Iriondo, A., and Kunk, M.J., 2015, Stratigraphy and structural development of the southwest Isla Tiburón marine basin: Implications for latest Miocene tectonic opening and flooding of the northern Gulf of California: Geosphere, v. 11, n. 4, doi: 10.1130 /GES01153.1.

Bennett, S.E.K., Darin, M.H., Dorsey, R.J., Skinner, L.A., Umhoefer, P.J., and Oskin, M.E., 2016, Animated tectonic reconstruction of the Lower Colorado River region: implications for Late Miocene to Present deformation, *in* 2016 Desert Symposium Field Guide and Proceedings, Zzyzx, California, California State University Desert Studies Center, p. 73-86.

Bird, P., 2009, Long-term fault slip rates, distributed deformation rates, and forecast of seismicity in the western United States from joint fitting of community geologic, geodetic, and stress direction data sets: Journal of Geophysical Research, v. 114, B11403, doi:10.1029/2009JB006317.

Buckland, K.N., Young, S.J., Keim, E.R., Johnson, B.R., Johnson, P.D., and Tratt, D.M, 2017, Tracking and quantification of gaseous chemical plumes from anthropogenic emission sources within the Los Angeles Basin: Remote Sensing of Environment, v. 201, p. 275- 296, doi: 10.1016/j.rse.2017.09.012.

Burbank, D.W., and Whistler, D.P., 1987, Temporally constrained tectonic rotations derived from magnetostratigraphic data: Implications for the initiation of the Garlock fault, California: Geology, v. 15, p. 1172-1175.

Carter, J.N., Luyendyk, B.P., and Terres, R.R., 1987, Neogene clockwise rotation of the eastern Transverse Ranges, California, suggested by paleomagnetic vectors: Geological Society of America Bulletin, v. 98, p. 199-206.

Chen, T., Akciz, S.O., Hudnut, K.W., Zhang, D.Z., and Stock, J.M., 2015, fault-slip distribution of the 1999 Mw 7.1 Hector Mine earthquake, California, estimated from postearthquake airborne LiDAR data: Bulletin of the Seismological Society of America, v. 105, no. 2A, p. 776-790, doi:10.1785/0120130108.

Christensen, P.R., and Harrison, S.T., 1993, Thermal infrared emission spectroscopy of natural surfaces: application to desert varnish coatings on rocks: Journal of Geophysical Research, v. 98, n. B11, p. 19819-19834.

Christensen, P.R., Bandfield, J.L., Hamilton, V.E., Howard, D.A., Lane, M.D., Piatek, J.L., Ruff, S.W., and Stefanov, W.L., 2000, A thermal emission spectral library of rock-forming minerals: Journal of Geophysical Research, v. 105, n. E4, p. 9735-9739.

Chuang, R.Y., and Johnson, K.M., 2011, Reconciling geologic and geodetic model fault slip-rate discrepancies in Southern California: Consideration of nonsteady mantle flow and lower crustal fault creep: Geology, v. 39; n. 7; p. 627-630, doi:10.1130/G32120.1.

Congalton, R.G., 1991, A review of assessing the accuracy of classifications of remotely sensed data: Remote Sensing of Environment, v. 37, p. 35-46, doi: 10.1016/0034-4257(91)90048-B.

Cooper, C.D., and Mustard, J.F., 1999, Effects of very fine particle size on reflectance spectra of smectite and palagonitic soil: Icarus, v. 142, p. 557-570, doi: 10.1006/icar.1999.6221.

Davis, G.A., and Burchfiel, B.C., 1973, Garlock fault, an intracontinental transform structure, southern California: Geological Society of America Bulletin, v. 84, p. 1407-1422, doi: 10.1130/0016-7606(1973)84<1407:GFAITS>2.0.CO;2.

Davis, G.H., Reynolds, S.J., and Kluth, C.F., 2012, Structural geology of rocks and regions, third edition: Hoboken, New Jersey, John Wiley & Sons, Inc., 839 p.

Dibblee, T.W., Jr., 1966, Geologic map of the Lavic quadrangle, San Bernardino County, California: U.S. Geological Survey Miscellaneous Geologic Investigations Map I-472, scale 1:62,500, 1 sheet.

Dibblee, T.W., Jr., 1967a, Geologic map of the Deadman Lake quadrangle, San Bernardino County, California: U.S. Geological Survey Miscellaneous Geologic Investigations Map I-488, scale 1:62,500, 1 sheet.

Dibblee, T.W., Jr., 1967b, Geologic map of the Emerson Lake quadrangle, San Bernardino County, California: U.S. Geological Survey Miscellaneous Geologic Investigations Map I-490, scale 1:62,500, 1 sheet.

Dibblee, T.W., Jr., 1967c, Geologic map of the Ludlow quadrangle, San Bernardino County, California: U.S. Geological Survey Miscellaneous Geologic Investigations Map I-477, scale 1:62,500, 1 sheet.

Dibblee, T.W., Jr., 2008, Geologic map of the Rodman Mountains and Lavic 15 minute quadrangles, San Bernardino County, California (edited by John A. Minch): Santa Barbara Museum of Natural History, Dibblee Geology Center Map #DF-378, scale 1:62,500, 1 sheet.

Dixon, T.H., Robaudo, S., Lee, J., and Reheis, M.C., 1995, Constraints on present-day Basin and Range deformation from space geodesy: Tectonics, v. 14, n. 4, p. 755-772, doi: 10.1029/95TC00931.

Dokka, R.K., 1983, Displacements on late Cenozoic strike-slip faults of the central Mojave Desert, California: Geology, v. 11, p. 305-308, doi: 10.1130/0091-7613(1983)11<305:DOLCSF>2.0.CO;2.

Dokka, R.K., and Travis, C.J., 1990a, Late Cenozoic strike-slip faulting in the Mojave Desert, California: Tectonics, v. 9, n. 2, p. 311-340, doi: 10.1029/TC009i002p00311.

Dokka, R.K., and Travis, C.J., 1990b, Role of the eastern California shear zone in accommodating Pacific-North American plate motion: Geophysical Research Letters, v. 17, n. 9, p. 1323- 1326, doi: 10.1029/GL017i009p01323.

Ferguson, C.A., McIntosh, W.C., and Miller, C.F., 2013, Silver Creek caldera-The tectonically dismembered source of the Peach Spring tuff: Geology, v. 41, n. 1, p. 3-6, doi:10.1130/G33551.1.

Fialko, Y., and Simons, M., 2001, The complete (3-D) surface displacement field in the epicentral area of the 1999 Mw 7.1 Hector Mine earthquake, California, from space geodetic observations: Geophysical Research Letters, v. 28, n. 16, p. 3063-3066, doi: 10.1029/2001GL013174.

Fossen, H. 2010, Structural geology: New York, Cambridge University Press, 463 p.

Friedrich, A.M., Wernicke, B.P., Niemi, N.A., Bennett, R.A., and Davis, J.L., 2003, Comparison of geodetic and geologic data from the Wasatch region, Utah, and implications for the spectral character of Earth deformation at periods of 10 to 10 million years: Journal of Geophysical Research, v. 118, n. B4, 2199, doi:10.1029/2001JB000682.

Gan, W., Zhang, P., and Shen, Z.-K., 2003, Initiation of deformation of the Eastern California Shear Zone: Constraints from Garlock fault geometry and GPS observations: Geophysical Research Letters, v. 30, n. 10, 1496, doi:10.1029/2003GL017090.

Garfunkel, Z., 1974, Model for the Late Cenozoic tectonic history of the Mojave Desert, California, and for its relation to adjacent regions: Geological Society of America Bulletin, v. 85, p. 1931-1944, doi: 10.1130/0016-7606(1974)85<1931:MFTLCT>2.0.CO;2.

Golombek, M.P., and Brown, L.L., 1988, Clockwise rotation of the western Mojave Desert: Geology, v. 16, p. 126-130, doi: 10.1130/0091-7613(1988)016<0126:CROTWM>2.3.CO;2.

Green, A.A., Berman, M., Switzer, P., and Craig, M.D., 1988, A transformation for ordering multispectral data in terms of image quality with implications for noise removal: IEEE Transactions on Geoscience and Remote Sensing, v. 26, no. 1, p. 65-74, doi: 10.1109/36.3001.

Hall, J.L., Boucher, R.H., Gutierrez, D.J., Hansel, S.J., Kasper, B.P., Keim, E.R., Moreno, N.M., Polak, M.L., Sivjee, M.G., Tratt, D.M., and Warren, D.W., 2011, First flights of a new

airborne thermal infrared imaging spectrometer with high area coverage, *in* Andresen, B.F., Fulop, G.F., and Norton, P.R., eds., Infrared Technology and Applications XXXVII, Proceedings of SPIE, v. 8012, p. 8012031-8012037, doi: 10.1117/12.884865.

Hector Mine Earthquake Geologic Working Group, 1999, Surface rupture, slip distribution, and other geologic observations associated with the M 7.1 Hector Mine earthquake of 16 October 1999 in AGU Fall Meeting Program, Dec. 13–17, 1999, p. 11.

Herbert, J.W., Cooke, M.L., Oskin, M., and Difo, O., 2014, How much can off-fault deformation contribute to the slip rate discrepancy within the eastern California shear zone?: Geology, v. 42, n. 1, p. 71-74, doi: 10.1130/G34738.1.

Hook, S.J., Dmochowski, J.E., Howard, K.A., Rowan, L.C., Karlstrom, K.E., and Stock, J.M., 2005, Mapping variations in weight percent silica measured from multispectral thermal infrared imagery—Examples from the Hiller Mountains, Nevada, USA, and Tres Virgenes-La Reforma, Baja California Sur, Mexico: Remote Sensing of Environment v. 95, p. 273-289, doi: 10.1016/j.rse.2004.11.020.

Horgan, B.H., Bell, J.F. III, Noe Dobrea, E.Z., Cloutis, E.A., Bailey, D.T., Craig, M.A., Roach, L.H., and Mustard, J.F., 2009, Distribution of hydrated minerals in the north polar region of Mars: Journal of Geophysical Research, v. 114, n. E01005, doi: 10.1029/2008JE003187.

Hudnut, K.W., Borsa, A., Glennie, C., and Minster, J.-B., 2002, High-resolution topography along surface rupture of the 16 October 1999 Hector Mine, California, earthquake (Mw 7.1) from airborne laser swath mapping: Bulletin of the Seismological Society of America, v. 92, n. 4, p. 1570-1576, doi: 10.1785/0120000934.

Jachens, R.C., Langenheim, V.E., and Matti, J.C., 2002, Relationship of the 1999 Hector Mine and 1992 Landers fault ruptures to offsets on Neogene faults and distribution of Late Cenozoic basins in the eastern California shear zone: Bulletin of the Seismological Society of America, v. 92, n. 4, p. 1592-1605, doi: 10.1785/0120000915.

Jagiello, K.J., 1991, Determination of horizontal separation on Late Cenozoic strike-slip faults in the central Mojave Desert, southern California [Ph.D. thesis]: Los Angeles, University of California, 293 p.

Johnson, A.M., Fleming, R.W., and Cruikshank, K.M., 1993, Broad belts of shear zones: The common form of surface rupture produced by the 28 June 1992 Landers, California, earthquake: United States Geological Survey Open-File Report 93-348, 29 p., doi: 10.2172/677052.

Johnson, K.M., 2013, Slip rates and off-fault deformation in southern California inferred from GPS data and models: Journal of Geophysical Research: Solid Earth, v. 118, p. 5643-5664, doi:10.1002/jgrb.50365.

Kealy, P.S., and Hook, S.J., 1993, Separating temperature and emissivity in thermal infrared multispectral scanner data: implications for recovering land surface temperatures: IEEE Transactions on Geoscience and Remote Sensing, v. 31, n. 6, p. 1155-1164, doi: 10.1109/36.317447.

Kirkland, L., Herr, K., Keim, E., Adams, P., Salisbury, J., Hackwell, J., and Treiman, A., 2001, First use of an airborne infrared hyperspectral scanner for compositional mapping: Remote Sensing of Environment, v. 80, p. 447-459, doi: 10.1016/S0034-4257(01)00323-6.

Kruse, F.A., Lefkoff, A.B., Boardman, J.W., Heidebrecht, K.B., Shapiro, A.T., Barloon, P.J., and Goetz, A.F.H., 1993, The Spectral Image Processing System (SIPS)-Interactive visualization and analysis of imaging spectrometer data: Remote Sensing of Environment, v. 44, p. 145-163, doi: 10.1016/0034-4257(93)90013-N.

Kruse, F.A., 1996, Geologic mapping using combined analysis of airborne visible/infrared imaging spectrometer (AVIRIS) and SIR-C/X-SAR data: Proceedings of SPIE, v. 2819, Imaging Spectrometry II, p. 24-35, doi: 10.1117/12.258078, event: SPIE's 1996 International Symposium on Optical Science, Engineering, and Instrumentation, Denver, Colorado, United States.

Kupfer, D.H., and Bassett, A.M., 1962, Geologic reconnaissance map of part of the southeastern Mojave Desert, California: United States Geological Survey Mineral Investigations Field Studies Map MF-205, scale 1:125,000.

Launer, P.J., 1952, Regularities in the infrared absorption spectra of the silicate minerals: American Mineralogist, v. 37, n. 9-10, p. 764-784, http://www.minsocam.org/ammin/AM37/AM37_764.pdf (accessed July 2018).

Le Bas, M.J., Le Maitre, R.W., Streckeisen, A., and Zanettin, B., 1986, A chemical classification of volcanic rocks based on the Total Alkali-Silica diagram: Journal of Petrology, v. 27, p. 745-750.

Lee, J.B., Woodyatt, S., and Berman, M., 1990, Enhancement of high spectral resolution remote- sensing data by a noise-adjusted principal components transform: IEEE Transactions on Geoscience and Remote Sensing, v. 28, n. 3, p. 295-304, doi: 10.1109/36.54356.

Luyendyk, B.P., Kamerling, M.J., and Terres, R., 1980, Geometric model for Neogene crustal rotations in southern California: Geological Society of America Bulletin, Part I, v. 91, n. 4, p. 211-217, doi: 10.1130/0016-7606(1980)91<211:GMFNCR>2.0.CO;2.

MacFadden, B.J., Woodburne, M.O., and Opdyke, N.D., 1990a, Paleomagnetism and Neogene clockwise rotation of the northern Cady Mountains, Mojave Desert of southern California: Journal of Geophysical Research, v. 95, n. B4, p. 4597-4608, doi: 10.1029/JB095iB04p04597.

MacFadden, B.J., Swisher, C.C. III, Opdyke, N.D., and Woodburne, M.O., 1990b, Paleomagnetism, geochronology, and possible tectonic rotation of the middle Miocene Barstow Formation, Mojave Desert, southern California: Geological Society of America Bulletin, v. 102, n. 4, p. 478-493, doi: 10.1130/0016-7606(1990)102<0478:PGAPTR>2.3.CO;2.

McClusky, S.C., Bjornstad, S.C., Hager, B.H., King, R.W., Meade, B.J., Miller, M.M., Monastero, F.C., and Souter, B.J., 2001, Present day kinematics of the eastern California shear zone from a geodetically constrained block model: Geophysical Research Letters, v. 28, n. 17, p. 3369-3372, doi: 10.1029/2001GL013091.

McGill, S.F., and Rubin, C.M., 1999, Surficial slip distribution on the central Emerson fault during the June 28, 1992, Landers earthquake, California: Journal of Geophysical Research, v. 104, n. B3, p. 4811-4833, doi: 10.1029/98JB01556.

McGill, S.F., Spinler, J.C., McGill, J.D., Bennett, R.A., Floyd, M.A., Fryxell, J.E., and Funning, G.J., 2015, Kinematic modeling of fault slip rates using new geodetic velocities from a transect across the Pacific-North America plate boundary through the San Bernardino Mountains, California: Journal of Geophysical Research: Solid Earth, v. 120, n. 4, doi:10.1002/2014JB011459.

McQuarrie, N., and Wernicke, B.P., 2005, An animated reconstruction of southwestern North America since 36 Ma: Geosphere, v. 1, n. 3, p. 147-172, doi: 10.1130/GES00016.1.

Meade, B.J., and Hager, B.H., 2005, Block models of crustal motion in southern California constrained by GPS measurements: Journal of Geophysical Research, v. 110, B03403, doi:10.1029/2004JB003209.

Miller, M.M., Johnson, D.J., Dixon, T.H., and Dokka, R.K., 2001, Refined kinematics of the eastern California shear zone from GPS observations, 1993-1998: Journal of Geophysical Research, v. 106, n. B2, p. 2245-2263, doi: 10.1029/2000JB900328.

Miller, D.M., and Yount, J.C., 2002, Late Cenozoic tectonic evolution of the north-central Mojave Desert inferred from fault history and physiographic evolution of the Fort Irwin area, California, *in* Glazner, A.F., Walker, J.D., and Bartley, J.M., eds., Geologic Evolution of the Mojave Desert and Southwestern Basin and Range: Boulder, Colorado, Geological Society of America Memoir 195, p. 173–197, doi: 10.1130/0-8137-1195-9.173.

Oskin, M., and Stock, J., 2003, Marine incursion synchronous with plate-boundary localization in the Gulf of California: Geology, v. 31, n. 1, p. 23-26, doi: 10.1130/0091-7613(2003)031<0023:MISWPB>2.0.CO;2.

Oskin, M., Perg, L., Shelef, E., Strane, M., Gurney, E., Singer, B., and Zhang, X., 2008, Elevated shear zone loading rate during an earthquake cluster in eastern California: Geology, v. 36, no. 6, p. 507-510, doi: 10.1130/G24814A.1.

Oskin, M., and Iriondo, A., 2004, Large-magnitude transient strain accumulation on the Blackwater fault, Eastern California shear zone: Geology, v. 32, n. 4, p. 313-316, doi: 10.1130/G20223.1.

Peltzer, G., Crampé, F., Hensley, S., and Rosen, P., 2001, Transient strain accumulation and fault interaction in the eastern California shear zone: Geology, v. 29, n. 11, p. 975-978, doi: 10.1130/0091-7613(2001)029<0975:TSAAFI>2.0.CO;2.

Phillips, F.M., 2003, Cosmogenic ^{36}Cl ages of Quaternary basalt flows in the Mojave Desert, California, USA: Geomorphology, v. 53, p. 199-208, doi:10.1016/S0169-555X(02)00328-8.

Plescia, J., and Henyey, T.L., 1982, Geophysical character of the proposed eastern extension of the Garlock fault and adjacent areas, eastern California: Geology, v. 10, p. 209-214, doi: 10.1130/0091-7613(1982)10<209:GCOTPE>2.0.CO;2.

QGIS Development Team, 2018, QGIS Geographic Information System, Open Source Geospatial Foundation Project: https://qgis.org/en/site/ (accessed September 2017).

Richard, S.M., 1993, Palinspastic reconstruction of southeastern California and southwestern Arizona for the Middle Miocene: Tectonics, v. 12, n. 4, p. 830-854, doi: 10.1029/92TC02951.

Richards, J.A., 2013, Remote Sensing Digital Image Analysis: An Introduction (Fifth Edition): Berlin, Germany, Springer-Verlag, 494 p., doi: 10.1007/978-3-642-30062-2.

Robitaille, P. -M., 2009, Kirchhoff's law of thermal emission: 150 years: Progress in Physics, v. 4, p. 3-13.

Rockwell, T.K., Lindvall, S., Herzberg, M., Murbach, D., Dawson, T., and Berger, G., 2000, Paleoseismology of the Johnson Valley, Kickapoo, and Homestead Valley faults: Clustering of earthquakes in the eastern California shear zone: Bulletin of the Seismological Society of America, v. 90, n. 5, p. 1200-1236, doi: 10.1785/0119990023.

Ross, T.M., Luyendyk, B.P., and Haston, R.B., 1989, Paleomagnetic evidence for Neogene clockwise tectonic rotations in the central Mojave Desert, California: Geology, v. 17, p. 470-473, doi: 10.1130/0091-7613(1989)017<0470:PEFNCT>2.3.CO;2.

Rymer, M.J., Seitz, G.G., Weaver, K.D., Orgil, A., Faneros, G., Hamilton, J.C., and Goetz, C., 2002, Geologic and paleoseismic study of the Lavic Lake fault at Lavic Lake playa, Mojave Desert, southern California: Bulletin of the Seismological Society of America, v. 92, n. 4, p. 1577-1591, doi: 10.1785/0120000936.

Salisbury, J.W., and Walter, L.S., 1989, Thermal infrared (2.5-13.5 μm) spectroscopic remote sensing of igneous rock types on particulate planetary surfaces: Journal of Geophysical Research, v. 94, n. B7, p. 9192-9202.

Salisbury, J.W., Wald, A., and D'Aria, D.M., 1994, Thermal-infrared remote sensing and Kirchhoff's law 1. Laboratory measurements: Journal of Geophysical Research, v. 99, n. B6, p. 11897-11911.

Sandwell, D.T., Sichoix, L., and Smith, B., 2002, The 1999 Hector Mine earthquake, southern California: Vector near-field displacements from ERS InSAR: Bulletin of the Seismological Society of America, v. 92, no. 4, p. 1341-1354, doi: 10.1785/0120000901.

Sauber, J., Thatcher, W., and Solomon, S.C., 1986, Geodetic measurement of deformation in the central Mojave Desert, California: Journal of Geophysical Research, v. 91, n. B12, p. 12,683-12,693, doi: 10.1029/JB091iB12p12683.

Sauber, J., Thatcher, W., Solomon, S.C., and Lisowski, M., 1994, Geodetic slip rate for the eastern California shear zone and the recurrence time of Mojave Desert earthquakes: Nature, v. 367, p. 264-266, doi: 10.1038/367264a0.

Savage, J.C., Lisowski, M., and Prescott, W.H., 1990, An apparent shear zone trending north-northwest across the Mojave Desert into Owens Valley, eastern California: Geophysical Research Letters, v. 17, n. 12, p. 2113-2116, doi: 10.1029/GL017i012p02113.

Savage, J.C., and Svarc, J.L., 1997, Postseismic deformation associated with the 1992 Mw = 7.3 Landers earthquake, southern California: Journal of Geophysical Research, v. 102, n.

B4, p. 7565-7577, doi: 10.1029/97JB00210.

Schermer, E.R., Luyendyk, B.P., and Cisowski, S., 1996, Late Cenozoic structure and tectonics of the northern Mojave Desert: Tectonics, v. 15, n. 5, p. 905-932, doi:10.1029/96TC00131.

Shelef, E., and Oskin, M., 2010, Deformation processes adjacent to active faults: Examples from eastern California: Journal of Geophysical Research, v. 115, B05308, doi:10.1029/2009JB006289.

Sieh, K., et al., 1993, Near-field investigations of the Landers earthquake sequence, April to July 1992: Science, v. 260, n. 5105, p. 171-176.

Simons, M., Fialko, Y., Rivera, L., 2002, Coseismic deformation from the 1999 Mw 7.1 Hector Mine, California, earthquake as inferred from InSAR and GPS observations: Bulletin of the Seismological Society of America, v. 92, no. 4, p. 1390-1402, doi: 10.1785/0120000933.

Snow, J.K., and Wernicke, B.P., 2000, Cenozoic tectonism in the central Basin and Range: magnitude, rate, and distribution of upper crustal strain: American Journal of Science, v. 300, p. 659-719.

Sousa, F.J., 2016, Tectonics of central and eastern California: Late Cretaceous to modern [Ph.D. thesis]: Pasadena, California Institute of Technology, 243 p., https://thesis.library.caltech.edu/9748/13/Sousa_Francis_2016_thesis.pdf (accessed July 2018).

Spinler, J.C., Bennett, R.A., Anderson, M.L., McGill, S.F., Hreinsdóttir, S., and McCallister, A., 2010, Present-day strain accumulation and slip rates associated with southern San Andreas and eastern California shear zone faults: Journal of Geophysical Research, v. 115, B11407, doi:10.1029/2010JB007424.

Spotila, J.A., and Sieh, K., 1995, Geologic investigations of a "slip gap" in the surficial ruptures of the 1992 Landers earthquake, southern California: Journal of Geophysical Research, v. 100, n. B1, p. 543-559, doi: 10.1029/94JB02471.

Stewart, J.H., 1983, Extensional tectonics in the Death Valley area, California: Transport of the Panamint Range structural block 80 km northwestward: Geology, v. 11, p. 153-157, doi: 10.1130/0091-7613(1983)11<153:ETITDV>2.0.CO;2.

Tou, J.T. and R. C. Gonzalez, 1974, Pattern Recognition Principles: Reading, Massachusetts, Addison-Wesley Publishing Company, 377 p.

Treiman, J.A., Kendrick, K.J., Bryant, W.A., Rockwell, T.K., and McGill, S.F., 2002, Primary surface rupture associated with the Mw 7.1 16 October 1999 Hector Mine

earthquake, San Bernardino County, California: Bulletin of the Seismological Society of America, v. 92, no. 4, p. 1171-1191, doi: 10.1785/0120000923.

Unruh, J.R., Lettis, W.R., and Sowers, J.M., 1994, Kinematic interpretation of the 1992 Landers earthquake: Bulletin of the Seismological Society of America, v. 84, n. 3, p. 537-546.

U.S. Geological Survey and California Geological Survey, 2006, Quaternary fault and fold database for the United States: http://earthquake.usgs.gov/hazards/qfaults/ (accessed September 2017).

Wells, R.E., and Hillhouse, J.W., 1989, Paleomagnetism and tectonic rotation of the lower Miocene Peach Springs Tuff: Colorado Plateau, Arizona, to Barstow, California: Geological Society of America Bulletin, v. 101, p. 846-863, doi: 10.1130/0016-7606(1989)101<0846:PATROT>2.3.CO;2.

Wessel, P., Smith, W.H.F, Scharroo, R., Luis, J., and Wobbe, F., 2013, Generic Mapping Tools: Improved Version Released: EOS, Transactions, American Geophysical Union, v. 94, no. 45, p. 409-410, doi: 10.1002/2013EO450001.

Woodburne, M.O., 2015, Mojave Desert Neogene tectonics and the onset of the eastern California shear zone, *in* Proceedings, 2015 Desert Symposium, Zzyzx, California, California State University Desert Studies Center, p. 153-199,

http://nsm.fullerton.edu/dsc/images/DSCdocs/DS%202015%20volume.pdf#page=153 (accessed July 2018).

Young, S.J., Johnson, B.R., and Hackwell, J.A., 2002, An in-scene method for atmospheric compensation of thermal hyperspectral data: Journal of Geophysical Research, v. 107, no. D24, p. 4774-4793, doi: 10.1029/2001JD001266.

Zachariasen, J., and Sieh, K., 1995, The transfer of slip between two en echelon strike- slip faults: A case study from the 1992 Landers earthquake, southern California: Journal of Geophysical Research, v. 100, n. B8, p. 15,281-15,301, doi: 10.1029/95JB00918.

FIGURE CAPTIONS

Figure 1 (p. 243): Overview map of the 1992 Mw 7.3 Landers and 1999 Mw 7.1 Hector Mine earthquake surface ruptures, and territory with access restricted by the MCAGCC (United States Marine Corps Air Ground Combat Center, Twentynine Palms) as of 1999 (solid line) and as of 2018 (dashed line). Other major faults shown are the Pinto Mountain fault (PMF) and the Mission Creek strand of the San Andreas fault (SAF). Base map is an SRTM 1 arc-second DEM hillshade (from the USGS Earth Resources Observation and Science website, https://eros.usgs.gov/, accessed on 09/02/2017). Faults are from U.S. Geological Survey and California Geological Survey (2006). Map was produced using QGIS software (QGIS, 2018).

Figure 2 (p. 244): (A) Overview of the Lavic Lake fault, mapped by its 1999 earthquake surface rupture. Arrows indicate relative fault motion, rectangular boxes are the extent of ground coverage of the hyperspectral airborne imagery used in this study, and LLP denotes the Lavic Lake playa, the geographic feature after which the fault is named (Hector Mine Earthquake Geologic Working Group, 1999). GIS data (base map and fault) is same as in Figure 1. Portions of other faults that ruptured in the 1999 earthquake are letter-coded as follows: CH- Calico-Hidalgo fault zone; ML- Mesquite Lake fault; BP- Bullion-Pisgah fault zone. (B) Overview of the portion of the Lavic Lake Fault covered by the hyperspectral airborne imagery footprints. "RF" denotes the Red Flake site, an area that was ground-truthed for supervised classifications. GIS data is same as in Figure 1. (C)-(F) Overview maps of the Red Flake site, centered at 34.586078° north, 116.288492° west. (C) Lidar 10 cm DEM hillshade (from the Open Topography website, http://www.opentopography.org/, accessed September 2017). Fault scarps from the 1999 earthquake are annotated by the dotted lines. (D) Polygon representing the area ground-truthed at the Red Flake site. Base map same as (C). (E) Elevation contour map of the Red Flake site (contour interval is 1 m). Polygon same as in (D). (F) Google Earth true color satellite image of the Red Flake site (imagery date: 2 January 2015). Polygon same as in (D). Maps in (A)-(E) were produced using QGIS software (QGIS, 2018).

Figure 3 (p. 245): Field photographs of the Red Flake site (located at 34.586078° north, 116.288492° west), an area where we ground-truthed the lithology as part of the supervised classification process. The lithologic variety at the Red Flake site is distinguishable by distinct differences in rock color, due to good exposure and little vegetative overgrowth. (A)

Overview facing west; circle denotes the location where the people seen in (C) are standing (photograph date / time / credit: 21 December 2012 / 9:49 am Pacific standard time / Joann Stock). (B) Overview facing north from helicopter; circle denotes location where the people seen in (C) are standing (photograph date / time / credit: 26 December 2012 / 1:14 pm Pacific standard time / Ken Hudnut). (C) View facing north of the 1999 earthquake fault scarp, showing the 1-m-tall protrusion of red feldspar porphyry (center of image, to right of scarp) from which the site derives its name. People on the horizon are circled for scale (photograph date / time / credit: 21 December 2012 / 10:30 am Pacific standard time / Ken Hudnut).

Figure 4 (p. 246): (A) Geologic map of the Red Flake site (located at 34.586078° north, 116.288492° west), with lithologic names and color assignments on the right. (B) Example of pixels randomly generated to produce end-member spectra for a supervised classification. Random generation is stratified (samples randomly chosen from individual classes) and proportionate to the area defined by a lithologic boundary (we used 2% of the area; e.g. if a certain lithology occupied 100 pixels of image area, two pixels would be randomly chosen for spectral sampling and averaged to define a representative end-member spectrum for said lithology. (C) Example remote sensing spectra derived from the randomly generated pixel selections shown in (B).

Figure 5 (p. 247): Thermal infrared laboratory spectra for lithologic hand samples collected at the Red Flake site. Spectra were measured on a Thermo-Nicolet 6700 FTIR Spectrometer using the biconical reflectance method. (A) Tuff and tuff breccia (four spectra), (B) detritus/colluvium (1 spectrum), (C) feldspar porphyry (3 spectra), and (D) microcrystalline

lava (2 spectra). All spectra were measured with a spot size of 1 - 2 mm, and each spectrum shown is an average of 150 scans taken over 4 - 6 minutes.

Figure 6 (p. 248): Data processing flowchart for our hyperspectral airborne image classifications. Based upon our knowledge of the site, we chose to perform standard classification techniques commonly available. We used the Environment for Visualizing Images Software, version 4.8 (ENVI, Exelis Visual Information Solutions, Boulder, Colorado). User-specified parameters are indicated by how they are input in dialogue boxes for each of the image processing steps. NESR- noise equivalent spectral radiance.

Figure 7 (p. 249): Overview of the complete hyperspectral airborne image swath, displayed in the following false color assignment: red, third MNF component; green, sixth MNF component; and blue, eighth MNF component. A subtle along-track gradation is present, and some clouds that were present during acquisition have been masked. The Red Flake site is annotated by a star, and located at 34.586078° north, 116.288492° west. Rectangular outline is the area shown in more detail in Figures 9, 10, and 11. GIS data is same as in Figure 1. Map was produced using QGIS software (QGIS, 2018).

Figure 8 (p. 250): (A)-(J) Ten supervised classifications of the Red Flake site (located at 34.586078° north, 116.288492° west). Lithologic contacts are superimposed for comparison with the ground-truthed geologic map (Figure 4A), and to visually assess the classification accuracy. Ground truth lithologic names, with color assignments, are shown at the bottom

for ready interpretation. Quantified results for the producer's, user's, and overall accuracies are in Tables 2 and 3, designated by the corresponding capital letters (A)-(J).

Figure 9 (p. 251): Geologic swath map of the Lavic Lake fault from an unsupervised classification of thermal hyperspectral airborne imagery. Thin lines are lithologic contacts; thick line is the approximate surface trace of the Lavic Lake fault (linework from Dibblee, 1966). Arrows indicate relative fault motion. Lithologic names shown in key are from correlating our classes with the units from Dibblee (also see Table 4). The Red Flake site is annotated by a star, and located at 34.586078° north, 116.288492° west. Upper right inset map (produced using Generic Mapping Tools, see Wessel et al., 2013) shows the footprint of the airborne imagery and the 1999 Hector Mine earthquake surface rupture (Treiman et al., 2002; U.S. Geological Survey and California Geological Survey, 2006). Lower left zoom inset (centered at 34.551116° north, 116.264804° west) shows a boundary between our classes that correlates well with a lithologic contact between tuff breccia and basalt (Dibblee, 1966). Note that some clouds that were present during image acquisition have been masked.

Figure 10 (p. 252): Portion of the Dibblee (1966) geologic map, zoomed to approximately the same area shown in the zoom inset of Figure 9. The map was modified by adding the line A-A' (with the representative cross section shown above the map), and also adding the asterisk symbol where the Tt/Tb contact was depicted as depositional, but is actually be a fault. The legend contains the relevant lithologic units and symbols featured here and discussed in the text. In the cross section, dip of the Tt/Tb depositional contact is from the

average of cross-section-projected dip domains on the east and west side of the Lavic Lake fault are 13º and 23º (both east/northeast), respectively.

Figure 11 (p. 253): Side-by-side comparison of the cumulative fault offset analysis area, as portrayed in (A) the MNF components in false color (from Figure 7), (B) the unsupervised classification (from Figure 9), and (C) the Dibblee (1966) map (from Figure 10). All panels are at the same scale (scale bar and north arrow in (A) apply to all three panels) and location (centered at 34.551116° north, 116.264804° west), with Dibblee's line work superimposed on the remote sensing imagery products in (A) and (B).

Figure 12 (p. 254): Oblique-view Google Earth satellite image (imagery date: 2 January 2015) of the location (centered at 34.551116° north, 116.264804° west) where we measured separation of piercing lines by the Lavic Lake fault (note that the scales are not accurate everywhere in the images, due to the oblique viewing geometry). (A) Image without annotation. (B) Thick black line is the Lavic Lake fault surface trace, thin red lines are Dibblee's Tt/Tb lithologic depositional contact, which separates the lighter-hued lithology (Tt, the older tuff breccia), from the darker-hued lithology (Tb, the younger basalt, which overlies Tt). (C) Thick black line is the Lavic Lake fault surface trace, thin green lines are the Tt/Tb depositional contact (modified from Dibblee's depiction), and the smaller cross faults are also depicted by a thick black line. We used the smaller cross faults to measure 930 m of horizontal, right-lateral map-view separation for the horizontal component of the slip vector. Note that the smaller cross fault on the west side of the Lavic Lake fault is depicted

in (B) as a portion of the Tt/Tb depositional contact. The yellow double-headed arrows white stars are the ground-based field photograph locations in Figure 13.

Figure 13 (p. 255): Ground-based field photographs of the cross fault (Tt/Tb fault contact) on the west side of the main Lavic Lake fault. Figure 12C shows the photograph locations as white stars. Person (Ken Hudnut) provides scale. (A) date: 3 April 2014; time: 4:09 pm Pacific daylight savings time; location: 34.556183º north, 116.267204º west; viewing direction: north/northwest; taken by Joann Stock. (B) date: 2 October 2012; time: 10:55 am Pacific daylight savings time; location: 34.557096º north, 116.266962º west; viewing direction: south/southwest; taken by Frank Sousa. (C) same as (A), but annotated with lithologic letter codes (see Table 4). (D) same as (B), but annotated with lithologic letter codes (see Table 4). In (A), bedding in Tt can be observed dipping to the east/northeast. In (C) and (D), note that the older Tt unit is structurally above the younger Tb unit.

TABLES

Table 1: ECSZ age of inception		
Author(s)	Age	Basis
Dokka and Travis (1990a; b)	6 - 10 Ma	Initiation of Garlock Fault c. 10 Ma (Burbank and Whistler, 1987), which is cut by younger ECSZ faults in the east (Davis and Burchfiel, 1973; Plescia and Henyey, 1982); age relations from Stewart (1983), which may indicate that some ECSZ faults initiated c. 6 Ma; Paleomagnetic data from Carter et al. (1987), which may indicate that regional deformation began after c. 6 Ma
Schermer et al. (1996)	<11.7 Ma	Fan deposits dated at 11.7 Ma have left lateral offset
Miller and Yount (2002)	>5 - 6 Ma	Left lateral faults controlled topography and subsequently the flow direction of 5-6 Ma basalts
Gan et al. (2003)	5.0 ± 0.4 Ma	Modeling the deflection of the Garlock Fault's once straight, but now curved surface trace
Oskin and Iriondo (2004)	>3.77 ± 0.11 Ma	Dated basalt flow that drapes a fault scarp in the Black Mountains
McQuarrie and Wernicke (2005)	c. 12 Ma	Right lateral shear, oriented N25°W since c. 12 Ma is based on palinspastic restoration modeling of mountain ranges in the southwestern U.S.A.
Woodburne (2015)	c. 6 Ma	Coupled with, or possibly as a byproduct of the opening of the Gulf of California (Atwater, 1992; Atwater and Stock, 1998; Oskin and Stock, 2003; Bennett et al., 2015); also cites a period of non-deposition in the Mojave Desert Region until c. 6 Ma to argue for tectonic quiescence up until that time.

Table 2: Red flake site supervised classification error matrices						
Classified	Ground truth				Total	User's accuracy
(A)	Tuff	Detritus	Feldspar porphyry	Microcrystalline lava		
Tuff	25	2	56	4	87	0.29
Detritus	11	28	69	3	111	0.25
Feldspar porphyry	13	0	125	89	227	0.55
Microcrystalline lava	13	0	112	747	872	0.86
Total possible	62	30	362	843	1297	
Producer's accuracy	0.40	0.93	0.35	0.89		Overall accuracy = 0.71
(B)						
Tuff	30	17	85	2	134	0.22
Detritus	2	3	12	0	17	0.18
Feldspar porphyry	18	10	161	121	310	0.52
Microcrystalline lava	12	0	105	719	836	0.86
Total possible	62	30	363	842	1297	
Producer's accuracy (%)	0.48	0.10	0.44	0.85		Overall accuracy = 0.70
(C)						
Tuff	41	6	97	24	168	0.24
Detritus	13	23	53	22	111	0.21
Feldspar porphyry	0	0	128	88	216	0.59
Microcrystalline lava	8	0	85	709	802	0.88
Total possible	62	29	363	843	1297	
Producer's accuracy (%)	0.66	0.79	0.35	0.84		Overall accuracy = 0.69
(D)						
Tuff	36	5	81	13	135	0.27
Detritus	4	24	43	1	72	0.33
Feldspar porphyry	9	0	114	68	191	0.60
Microcrystalline lava	13	0	124	761	898	0.85
Total possible	62	29	362	843	1296	
Producer's accuracy (%)	0.58	0.83	0.31	0.90		Overall accuracy = 0.72
(E)						
Tuff	13	2	26	7	48	0.27
Detritus	29	24	87	2	142	0.17
Feldspar porphyry	11	3	117	59	190	0.62

Microcrystalline lava	8	0	132	775	915	0.85
Total possible	61	29	362	843	1295	
Producer's accuracy (%)	0.21	0.83	0.32	0.92		Overall accuracy = 0.72
(F)						
Tuff	19	1	44	61	125	0.15
Detritus	28	24	103	5	160	0.15
Feldspar porphyry	1	5	124	45	175	0.71
Microcrystalline lava	14	0	92	731	837	0.87
Total possible	62	30	363	842	1297	
Producer's accuracy (%)	0.31	0.80	0.34	0.87		Overall accuracy = 0.69
(G)						
Tuff	28	1	70	36	135	0.21
Detritus	23	26	68	5	122	0.21
Feldspar porphyry	1	3	109	45	158	0.69
Microcrystalline lava	10	0	116	756	882	0.86
Total possible	62	30	363	842	1297	
Producer's accuracy (%)	0.45	0.87	0.30	0.90		Overall accuracy = 0.71
(H)						
Tuff	15	4	20	7	46	0.33
Detritus	22	16	86	3	127	0.13
Feldspar porphyry	10	10	133	63	216	0.62
Microcrystalline lava	15	0	124	769	908	0.85
Total possible	62	30	363	842	1297	
Producer's accuracy (%)	0.24	0.53	0.37	0.91		Overall accuracy = 0.72
(I)						
Tuff	15	1	27	22	65	0.23
Detritus	34	23	98	11	166	0.14
Feldspar porphyry	4	6	116	55	181	0.64
Microcrystalline lava	8	0	122	755	885	0.85
Total possible	61	30	363	843	1297	
Producer's accuracy (%)	0.25	0.77	0.32	0.90		Overall accuracy = 0.70
(J)						
Tuff	16	1	26	10	53	0.30
Detritus	22	20	83	6	131	0.15

Feldspar porphyry	9	8	101	37	155	0.65
Microcrystalline lava	15	0	152	790	957	0.83
Total possible	62	29	362	843	1296	
Producer's accuracy (%)	0.26	0.69	0.28	0.94		Overall accuracy = 0.72

Table 3: Red flake site supervised classification accuracy summary*				
Lithology	# of 4-m^2 pixels	Area (m^2)	Producer's accuracy (%)	User's accuracy (%)
Tuff (and tuff breccia)	62	248	38 ± 16	25 ± 5
Detritus (colluvium)	30	120	71 ± 24	19 ± 6
Feldspar porphyry	364	1456	34 ± 4	62 ± 6
Microcrystalline lava	845	3380	89 ± 3	86 ± 1
*Standard deviation = 1σ; all values rounded to nearest integer				

Table 4: Correlation of unsupervised classification units with lithologic units from the Dibblee (1966) geologic map[1]			
Class color	Lithologic name given here	Letter codes and lithologic names from Dibblee (1966)[2]	Class also includes these units[2]
Yellow	Alluvium	Qa: alluvium Qf: fan gravel Qoa: older alluvium Qof*: older valley sediments, fanglomerate and gravel	QTr: rhyolitic felsite, (and all others)
Red	Felsite	Tif: intrusive felsite	Ta, Tt
Magenta	Andesite	Ta*: andesite Tap: andesite porphyry Tfa: fanglomerate of andesitic detritus	Qof, QTr, Tif, Tb, Tt
Purple	Weathered basalt	Tb*: basalt Tib: intrusive basalt	Tt
Blue	Basalt	Tb*: basalt Tib: intrusive basalt	QTr, Ta, Tt
Green	Tuff breccia	Tt: tuff breccia	Qof, Tif, Ta

[1]See Dibblee (1966; 1967abc; 2008) for complete lithologic descriptions; correlations are broad generalizations that do not necessarily cover every possible detail/variation

[2]Q: Quaternary, T: Tertiary; when multiple units appear in column three, asterisks indicate the predominant correlative unit

Table 5: Unsupervised classification error matrix for the Red flake site					
Classified	Ground truth			Total	User's accuracy
	Tuff	Detritus	Other		
Tuff	41	7	99	147	0.28
Detritus	1	20	351	372	0.05
Other	13	0	631	644	0.98
Total Possible	55	27	1081	1163	
Producer's accuracy	0.75	0.74	0.58		Overall accuracy = 0.60

FIGURES

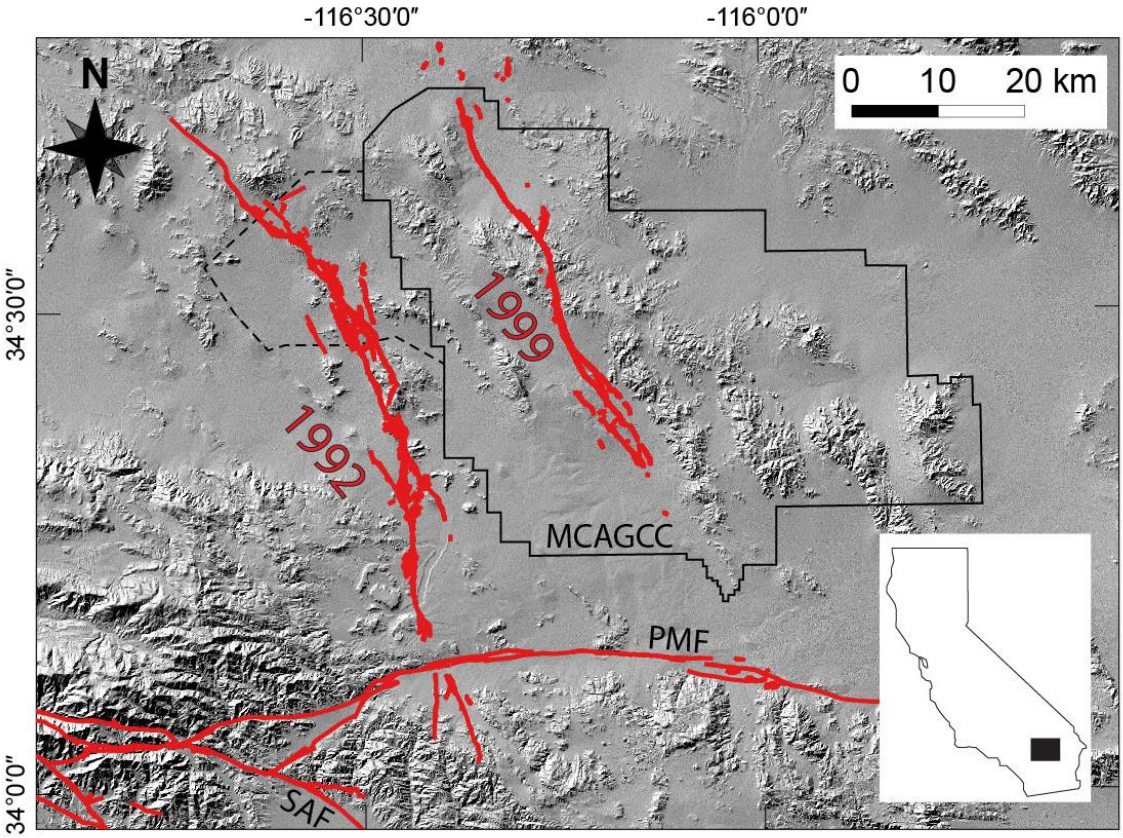

Figure 1

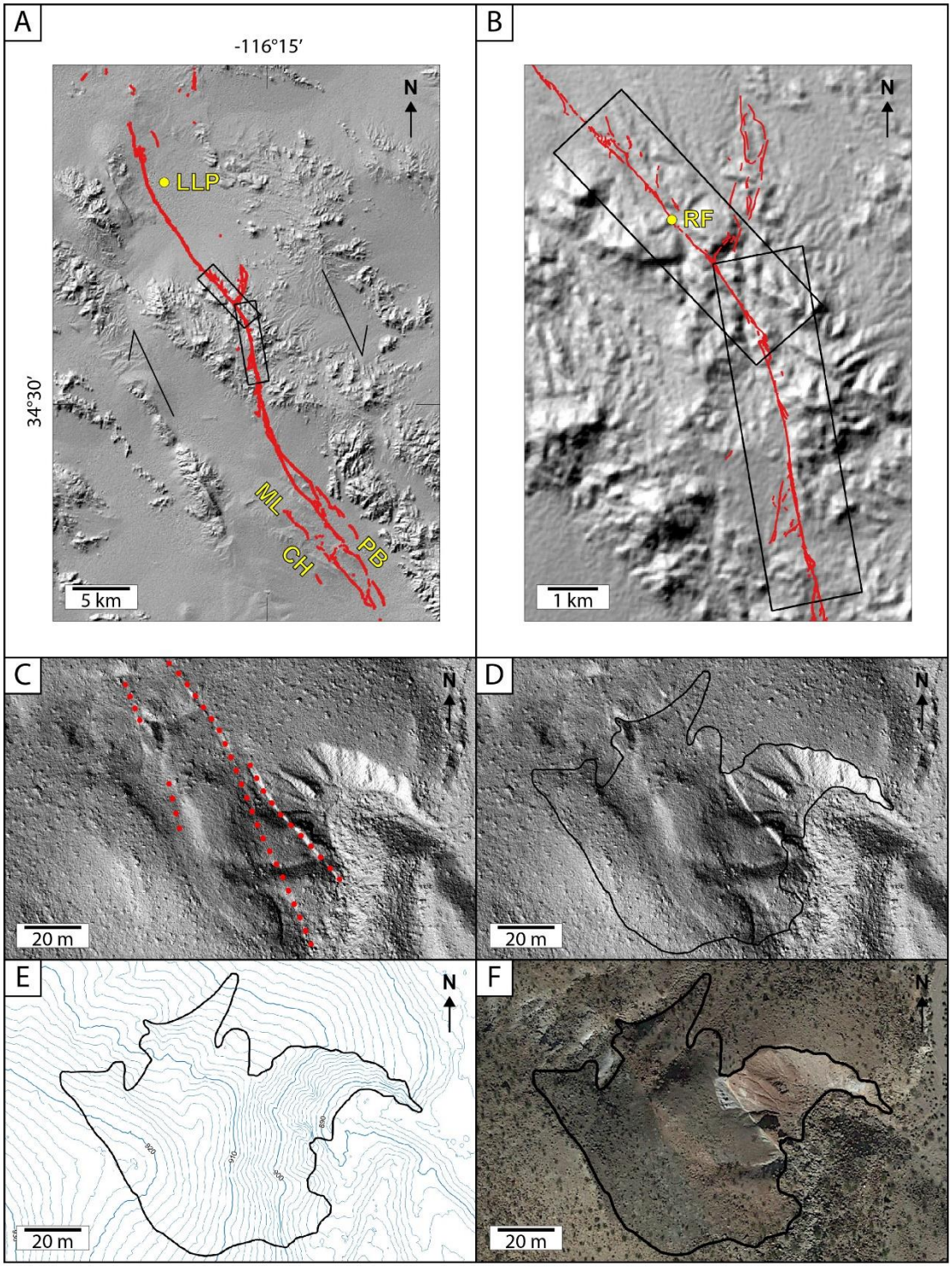
A
-116°15′
34°30′
N
LLP
ML
CH
PB
5 km
B
N
RF
1 km
C
N
20 m
D
N
20 m
E
N
20 m
F
N
20 m

Figure 2

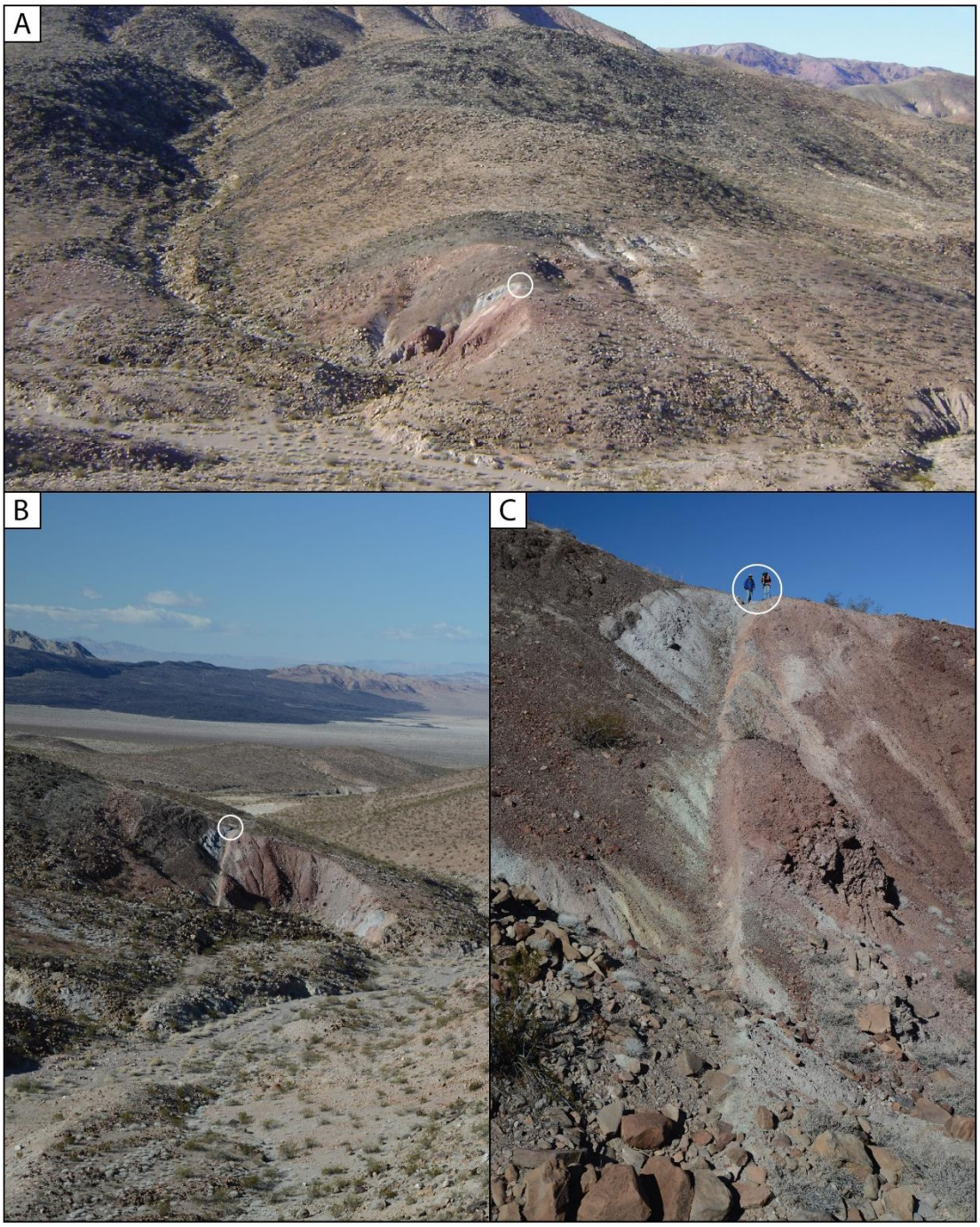

Figure 3

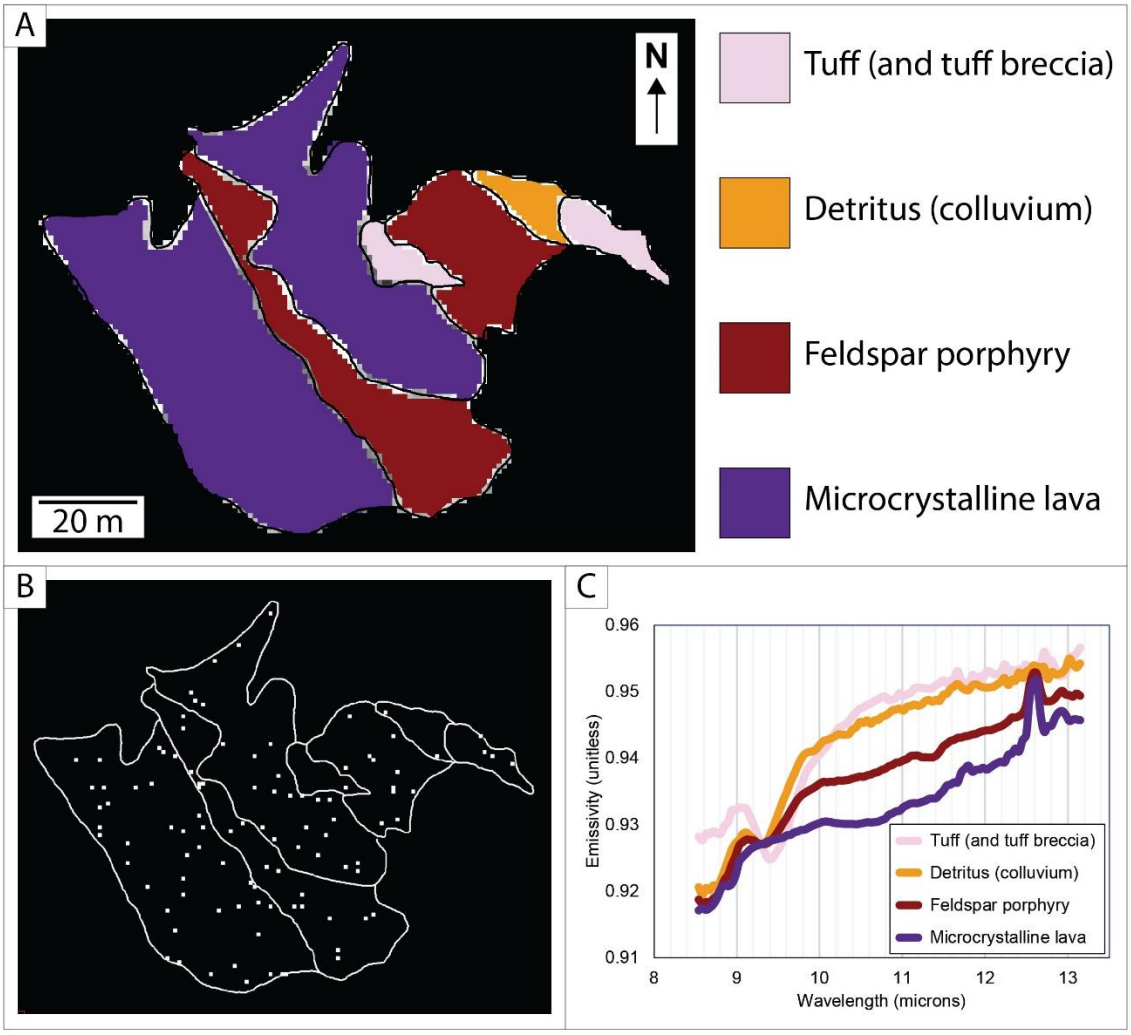
A
N
20 m
Tuff (and tuff breccia)
Detritus (colluvium)
Feldspar porphyry
Microcrystalline lava
B
C
0.96
0.95
0.94
0.93
0.92
0.91
Emissivity (unitless)
8
9
10
11
12
13
Wavelength (microns)
Tuff (and tuff breccia)
Detritus (colluvium)
Feldspar porphyry
Microcrystalline lava

Figure 4

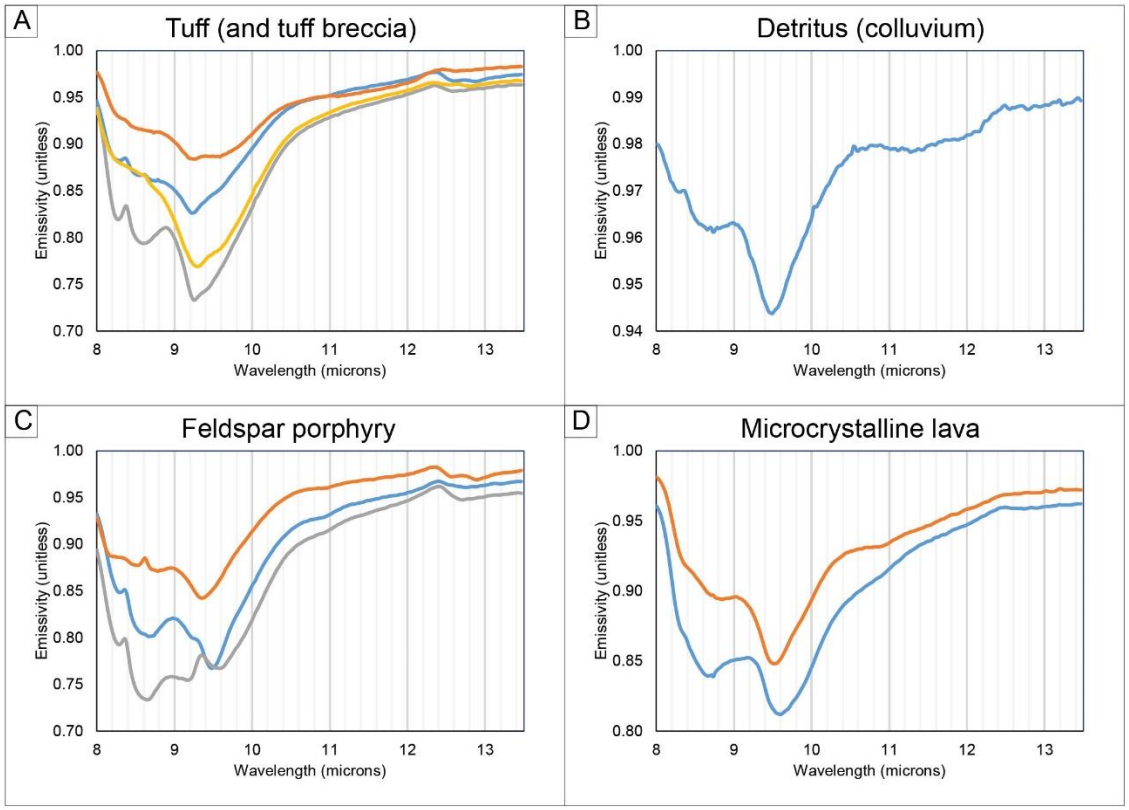
A
Tuff (and tuff breccia)
Emissivity (unitless)
1.00
0.95
0.90
0.85
0.80
0.75
0.70
8
9
10
11
12
13
Wavelength (microns)
B
Detritus (colluvium)
Emissivity (unitless)
1.00
0.99
0.98
0.97
0.96
0.95
0.94
8
9
10
11
12
13
Wavelength (microns)
C
Feldspar porphyry
Emissivity (unitless)
1.00
0.95
0.90
0.85
0.80
0.75
0.70
8
9
10
11
12
13
Wavelength (microns)
D
Microcrystalline lava
Emissivity (unitless)
1.00
0.95
0.90
0.85
0.80
8
9
10
11
12
13
Wavelength (microns)

Figure 5

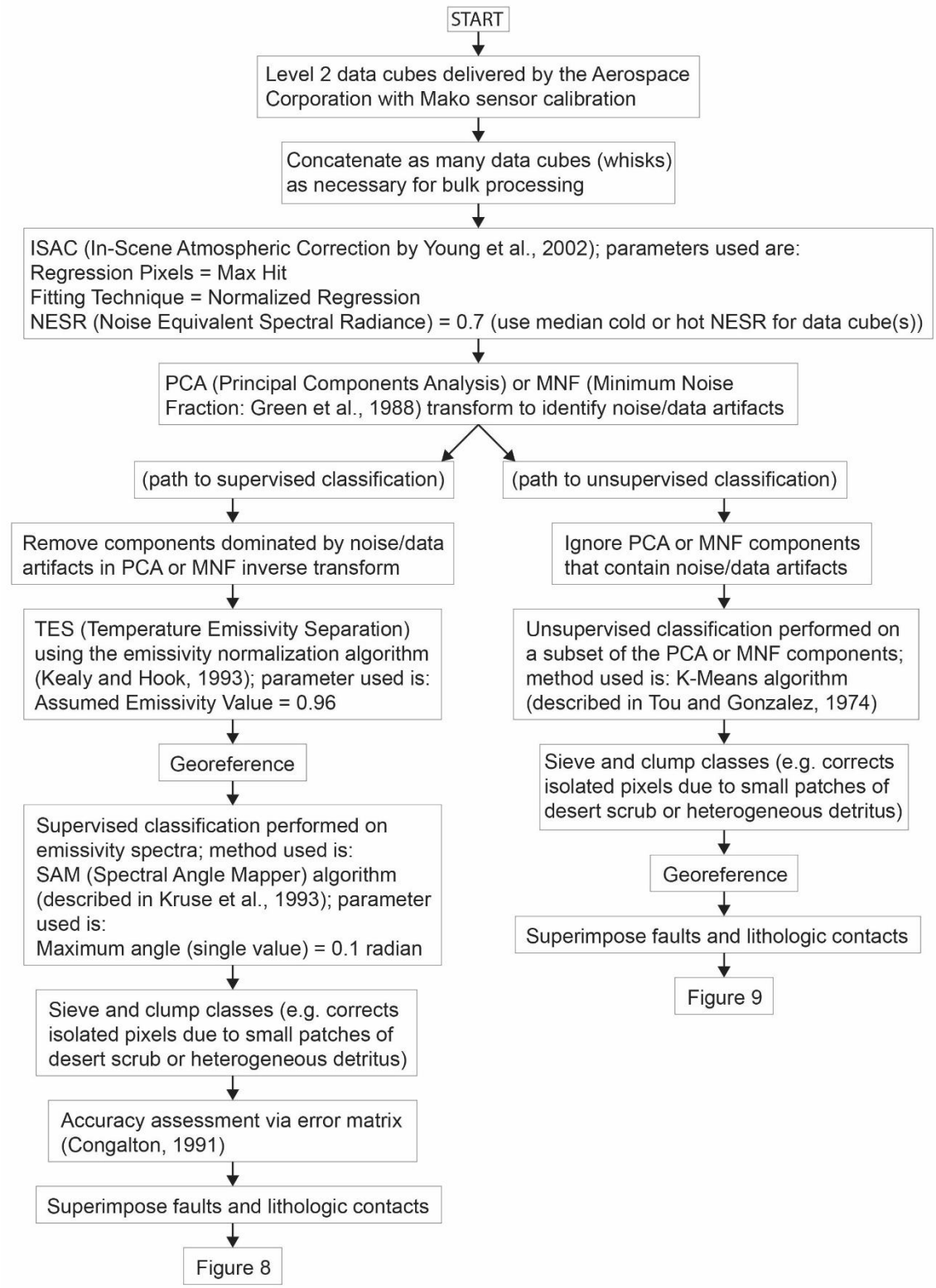
START
Level 2 data cubes delivered by the Aerospace Corporation with Mako sensor calibration
Concatenate as many data cubes (whisks) as necessary for bulk processing
ISAC (In-Scene Atmospheric Correction by Young et al., 2002); parameters used are:
Regression Pixels = Max Hit
Fitting Technique = Normalized Regression
NESR (Noise Equivalent Spectral Radiance) = 0.7 (use median cold or hot NESR for data cube(s))
PCA (Principal Components Analysis) or MNF (Minimum Noise Fraction: Green et al., 1988) transform to identify noise/data artifacts
(path to supervised classification)
(path to unsupervised classification)
Remove components dominated by noise/data artifacts in PCA or MNF inverse transform
Ignore PCA or MNF components that contain noise/data artifacts
TES (Temperature Emissivity Separation) using the emissivity normalization algorithm (Kealy and Hook, 1993); parameter used is:
Assumed Emissivity Value = 0.96
Unsupervised classification performed on a subset of the PCA or MNF components; method used is: K-Means algorithm (described in Tou and Gonzalez, 1974)
Georeference
Sieve and clump classes (e.g. corrects isolated pixels due to small patches of desert scrub or heterogeneous detritus)
Supervised classification performed on emissivity spectra; method used is:
SAM (Spectral Angle Mapper) algorithm (described in Kruse et al., 1993); parameter used is:
Maximum angle (single value) = 0.1 radian
Georeference
Sieve and clump classes (e.g. corrects isolated pixels due to small patches of desert scrub or heterogeneous detritus)
Superimpose faults and lithologic contacts
Accuracy assessment via error matrix (Congalton, 1991)
Figure 9
Superimpose faults and lithologic contacts
Figure 8

Figure 6

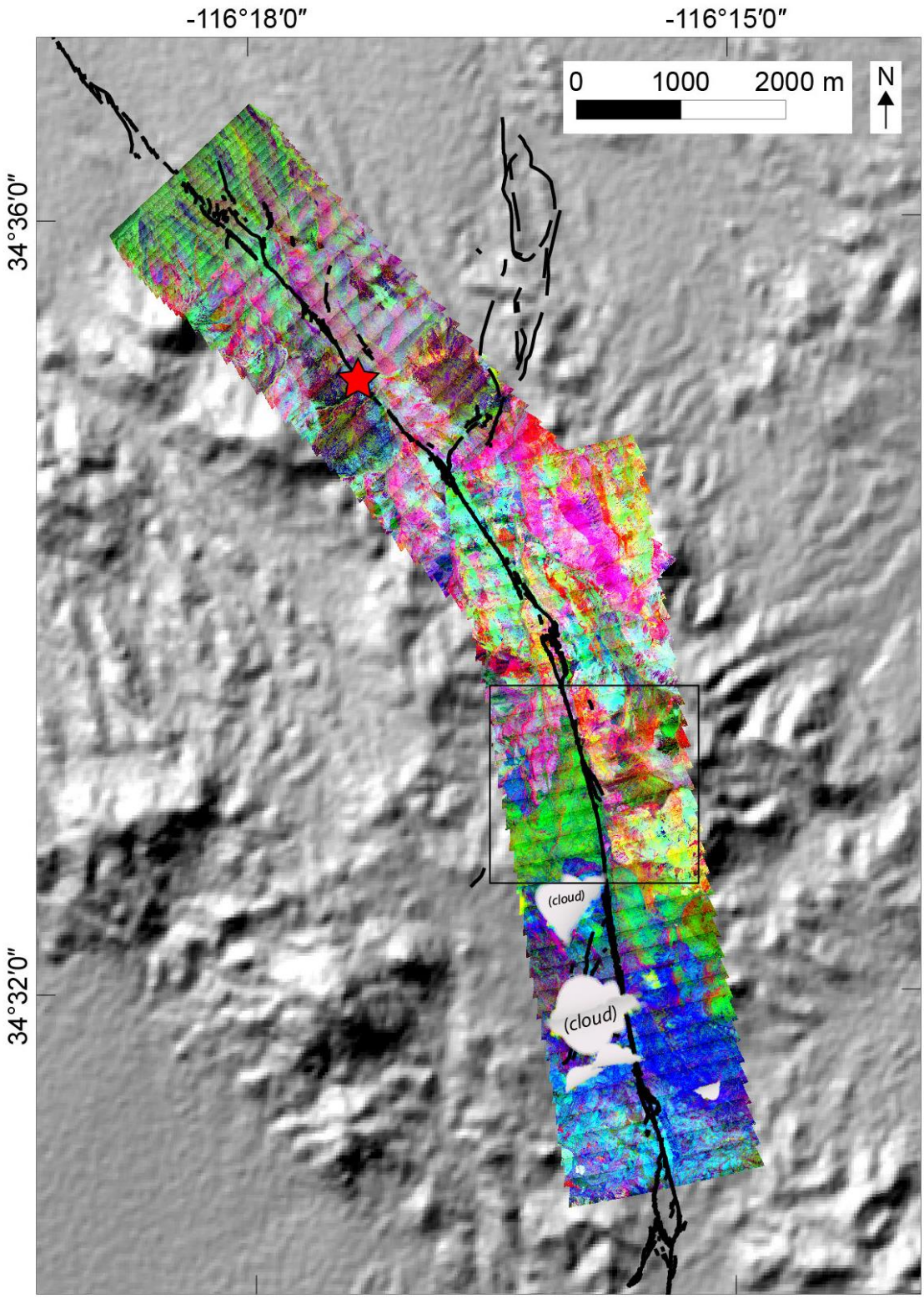

Figure 7

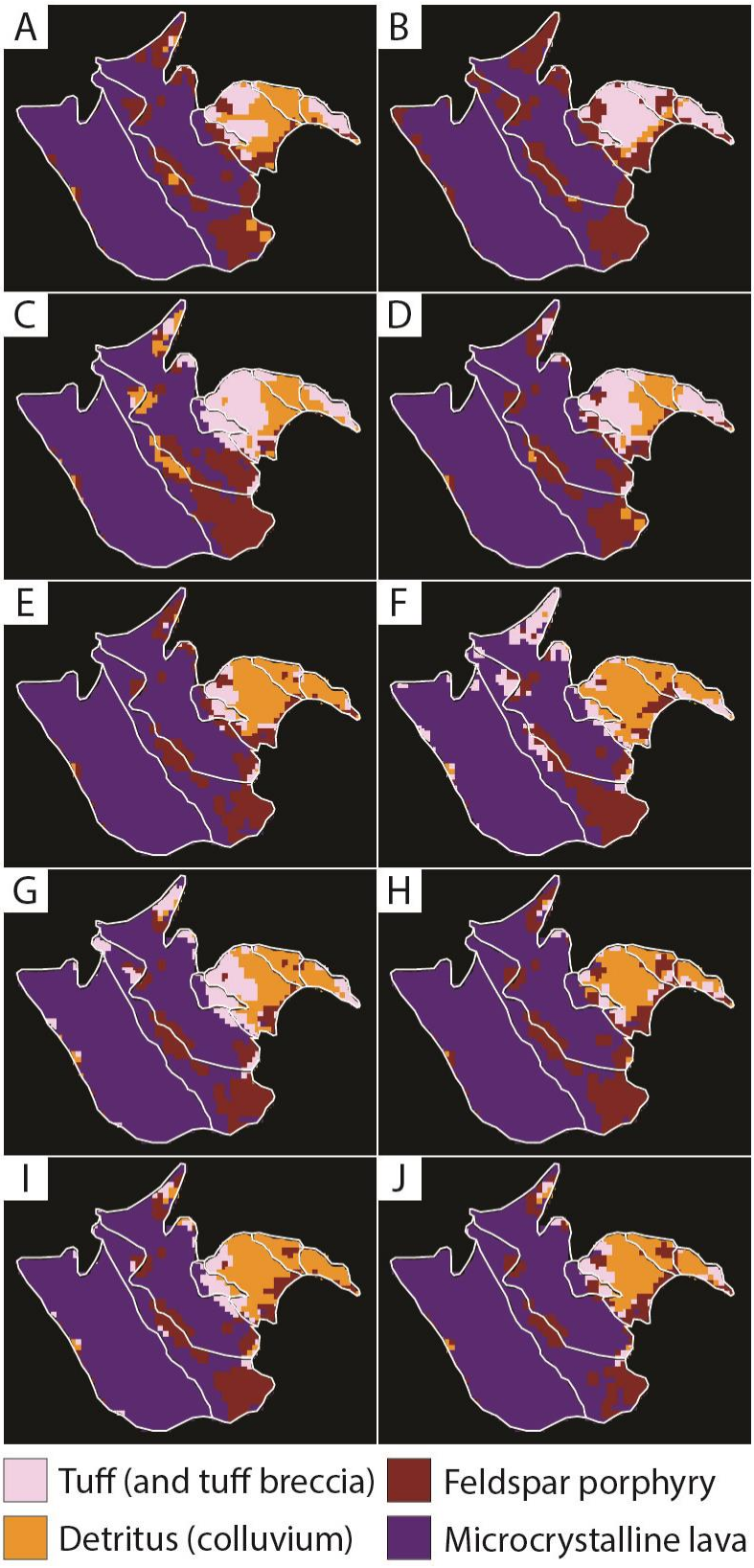
A
B
C
D
E
F
G
H
I
J
Tuff (and tuff breccia)
Feldspar porphyry
Detritus (colluvium)
Microcrystalline lava

Figure 8

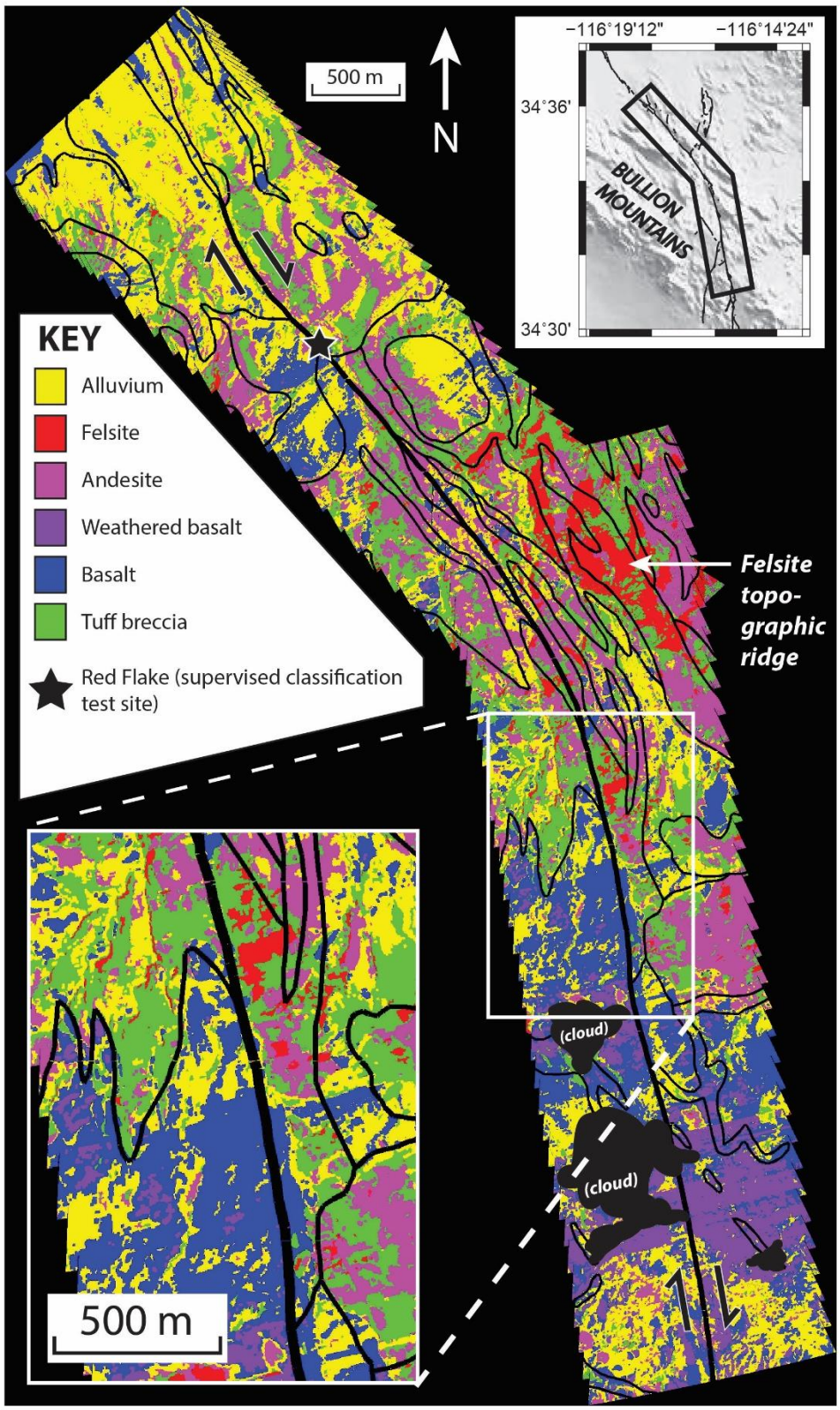
500 m
N
−116°19'12"
−116°14'24"
34°36'
34°30'
BULLION MOUNTAINS
KEY
Alluvium
Felsite
Andesite
Weathered basalt
Basalt
Tuff breccia
Red Flake (supervised classification test site)
Felsite topo-graphic ridge
(cloud)
(cloud)
500 m

Figure 9

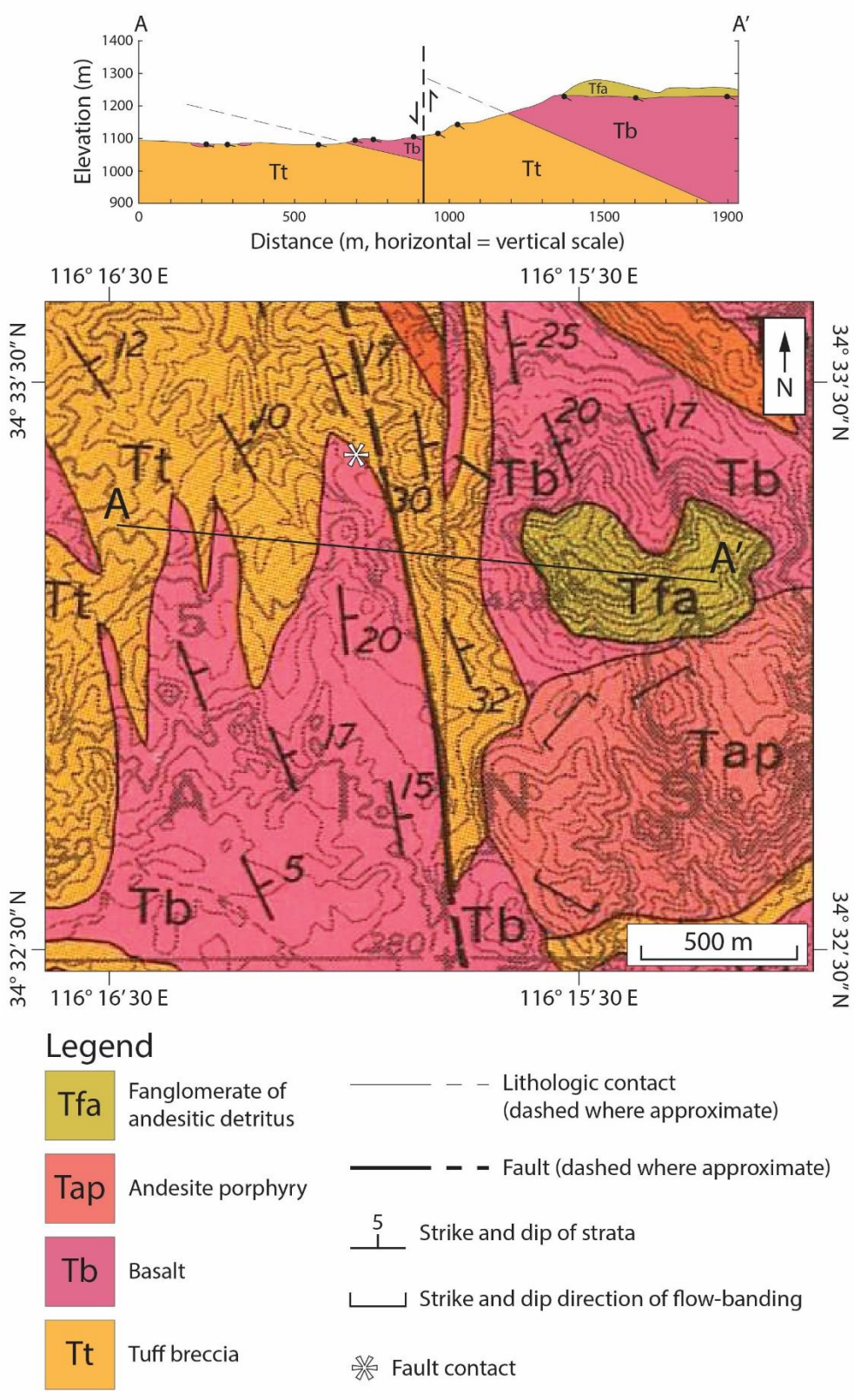
A
A′
Elevation (m)
1400
1300
1200
1100
1000
900
0
500
1000
1500
1900
Tfa
Tb
Tt
Tb
Tt
Distance (m, horizontal = vertical scale)
116° 16′ 30 E
116° 15′ 30 E
34° 33′ 30″ N
34° 32′ 30″ N
N
Tt
Tb
Tfa
Tap
A
A′
500 m
Legend
Tfa
Fanglomerate of andesitic detritus
Tap
Andesite porphyry
Tb
Basalt
Tt
Tuff breccia
Lithologic contact (dashed where approximate)
Fault (dashed where approximate)
Strike and dip of strata
Strike and dip direction of flow-banding
Fault contact

Figure 10

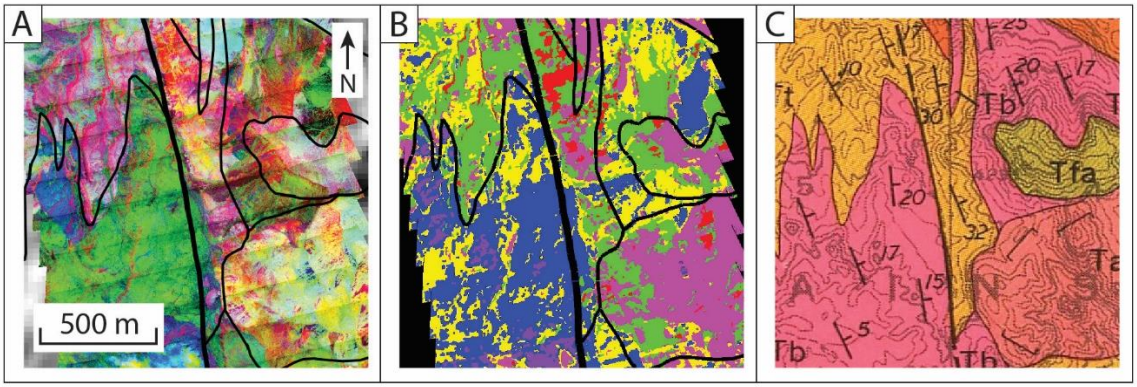

Figure 11

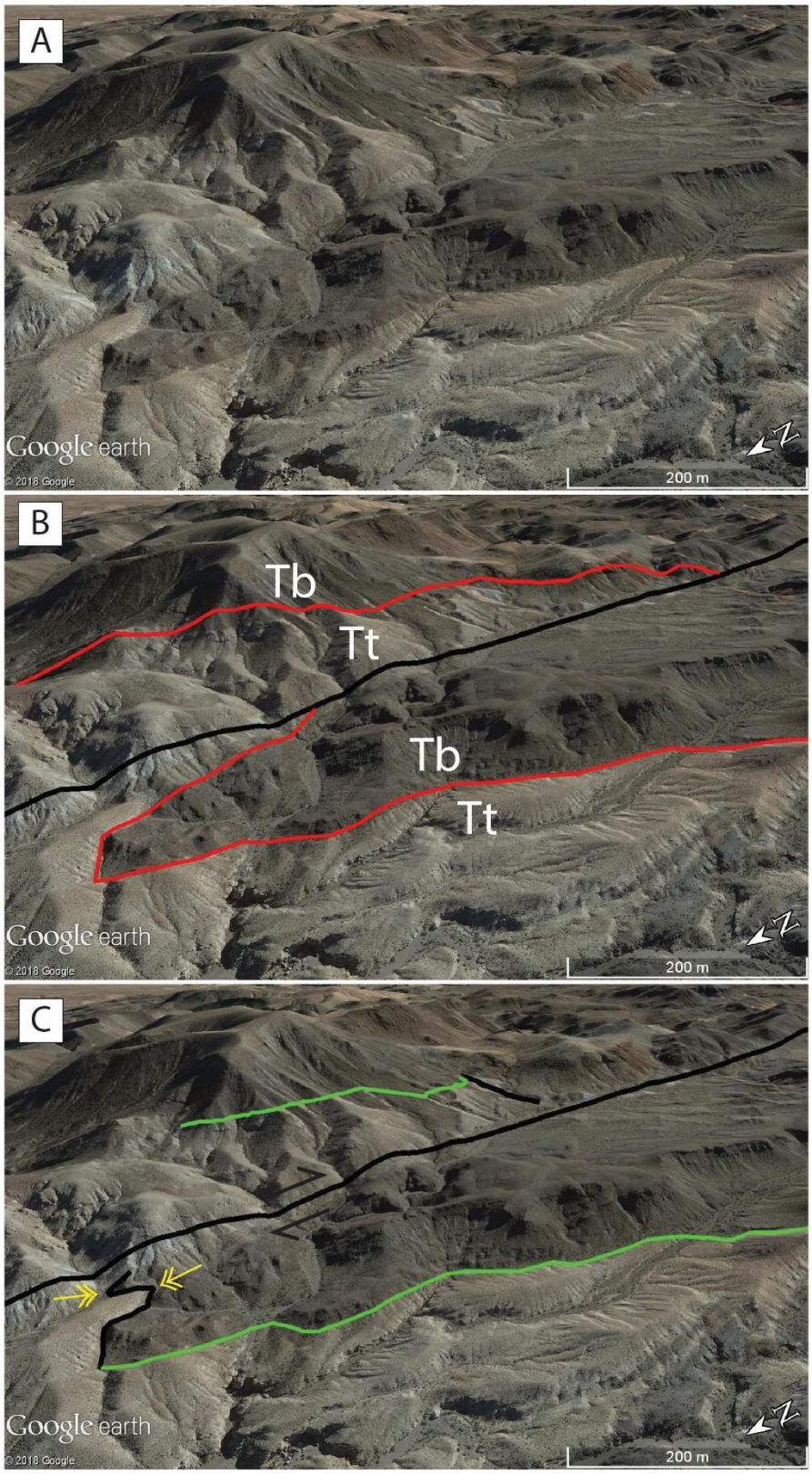
A
Google earth
© 2018 Google
200 m
N
B
Tb
Tt
Tb
Tt
Google earth
© 2018 Google
200 m
N
C
Google earth
© 2018 Google
200 m
N

Figure 12

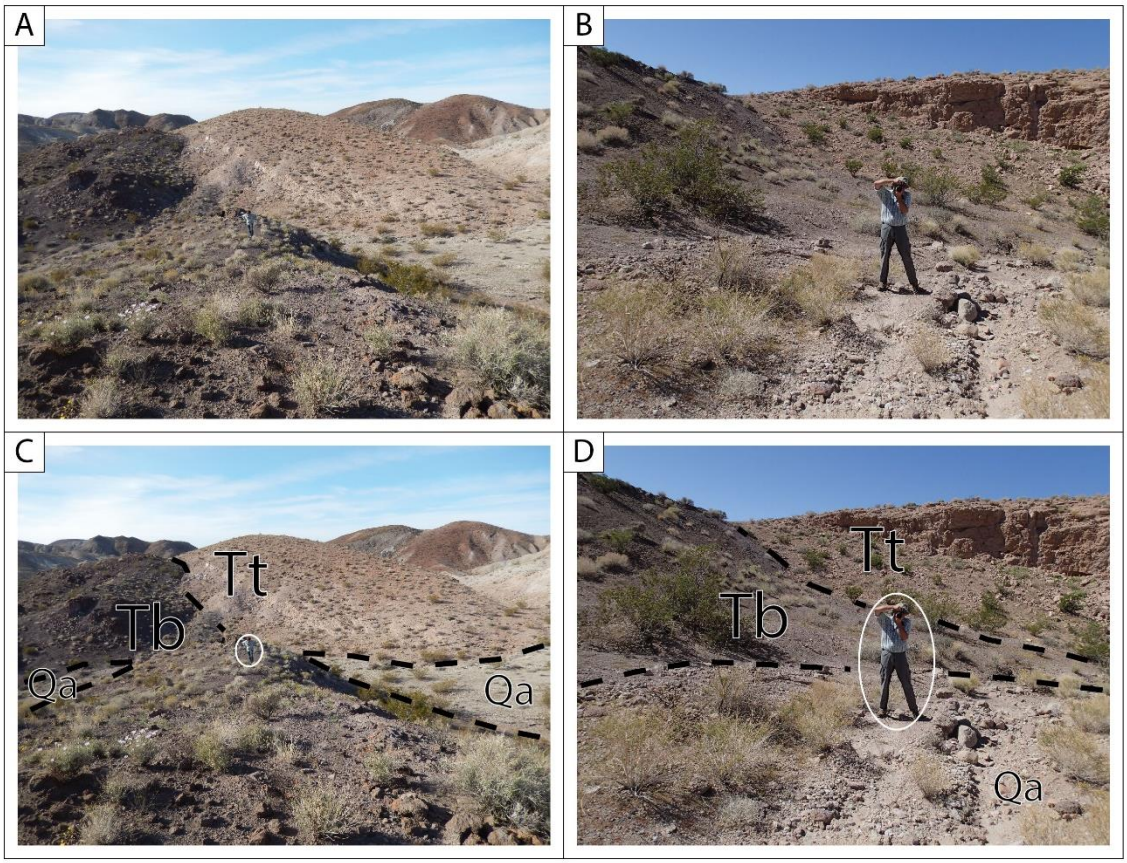

Figure 13